Chapter 2

Modeling and Testing the Effect of Cell Size on Auxin Distribution

2.1 Introduction

In the 19th century, Charles Darwin was the first to propose that phototropism is caused by a transmissible substance which was later discovered by Kogl and Haagen-Smit and named auxin [1, 2]. Since then, auxin was determined to be a class of compounds comprised of an aromatic ring and a carbolxylic acid moiety that all have similar phenotypic effects on plants.

This hormone family is now known to be involved in the morphogenesis of many different organs and tissues within Arabidopsis. Members of this family are generally thought to move between cells through both diffusion and active transport and cause proliferation and differentiation where it accumulates in high concentration. This property of auxin is of particular interest because it provides a mechanism for explaining the formation of organs at particular, periodic locations even if the underlying mechanism of auxin transport is not fully understood. And the knowledge that we *do* have about auxin transport has allowed us, in the work described here, to create models that in some instances make accurate predictions about the phenotypes of various mutants. But in order to make such models, we first must understand some of the fundamentals of auxin biochemistry and auxin's role in tissue differentiation.

The transport of auxin through tissue is the focus of this work, but other aspects of auxin biochemistry are just as important during auxin-induced morphogenesis such as biosynthesis, metabolism, and sensing. The details of these processes are critical for the higher-order patterns spanning cells and organs. I this section I will first cover the basics of auxin synthesis, then the mechanisms of auxin transport, and finally the propagation of the auxin signal to the extent that it alters gene expression.

2.1.1 Synthesis

The most commonly studied member of the auxin family is Indole-3-acetic acid (IAA), which is found in concentrations as high as 250pg·mg^{-1} in mature leaves, cotyledons, and both shoot and root meristem tissue[3, 4]. There are three known, independent pathways for synthesizing IAA. The first to be discovered was the tryptophan dependent pathway, although isotope labelling experiments showed that this was not the only pathway[5]. Initially this was thought to be the primary mechanism by which IAA is synthesized but experiments involving TRP2 and TRP3 mutants (mutants for tryptophan biosynthesis) showed similar or even *increased* levels of IAA compared to wild type tissue[6].

Once some of proteins required for IAA synthesis became known it became obvious that there were at least two distinct pathways. One of these pathways starts with indole-3-glycerol phosphate as a precursor while the other uses a tryptophan (Trp) precursor[7]. When radioisotope labelled tryptophan and anthranilate were introduced to trp2-1 (10% of wild type tryptophan production) mutants, mass spec isotope analysis of tryptophan showed that the majority of IAA was being produced independent of the labeled tryptophan[5]. Additional evidence of a tryptophan independent pathway was that in tryptophan synthesis mutants such as trp3-1 and trp2-1 the concentration of IAA is similar to that of wild type plants. Indole-3-glycerol phosphate was identified as the secondary pathway when indole-3-glycerol phosphate synthase antisense RNAs were introduced to trp2-1 and trp3-1 mutants and the resulting plants showed auxin deficient characteristics[6].

Today it is known that there are two distinct tryptophan independent IAA synthesis pathways. One of those pathways uses indole-3-acetaldoxime (IAOx) and the other, indole-3-pyruvate (IPA). The indole-3-acetaldoxime pathway is carried out by the two P450 monooxygenases CYP79B2 and CYP79B4[8, 9, 10, 11], although this pathway may be limited to the Brassicales and not play a major part in auxin synthesis across all plants[12]. The other pathway involving IPA is probably more widely used throughout the plant kingdom and recently has been characterized. Genetic screens have identified an aminotransferase that is responsible for catalyzing the synthesis of indole-3-acetaldehyde from IPA[13, 14]. Plants carrying mutations in this aminotransferase look similar to auxin signalling mutants and have severe early development phenotypes[13]. IAA can also be synthesized from IPA through flavin monooxygenase enzymes in the YUCCA family[15]. Over expression of these monooxygenase genes results in an increased concentration of indole-3-acetic acid[13, 16, 17, 18]. Additionally, these monooxygenases have been determined to be the rate limiting step in the IPA dependent pathway[19] and are tightly regulated with multiple redundancies[20, 21, 22, 23].

Even though the synthetic pathways for auxin synthesis have been extensively probed, the exact locations with the plant, tissue, and cellular organelles are still mysterious. In the model used in this study, auxin is assumed to be produced uniformly throughout the tissue at a steady rate and without regard to the subcellular localization. But in order the better understand the mechanisms by which auxin controls plant development, more work will be needed to characterize the spatial and temporal expression of the many genes involved in these synthetic pathways.

2.1.2 Transport

In Arabidopsis, auxin is known to be distributed through three distinct mechanisms regardless of the synthetic pathway or location of synthesis: diffusion through cytoplasm and extracellular space, transport (active and passive) across plasma membranes, and movement (diffusion and bulk transport) through vascular tissue. Looking specifically at cross-membrane movement, auxin is often transported in a polarized fashion. This polar auxin transport is critical both for generating local auxin maxima and in long distance transport. This transport occurs in a manner that depends on plasma membrane-localized proteins facilitating the movement of auxin from the cytoplasm to the apoplasm and vice versa. Many auxin carriers are well characterized: the PIN proteins[24] and several proteins of the ABCG and ABCB transporter family[25, 26, 27] are involved in auxin efflux from the cell and the AUX1 and LAX proteins are involved in auxin influx [28, 29].

While there are many proteins that transport auxin across membranes, the rate limiting step in polar auxin transport was determined to be the proteins in the PIN family[30, 31]. In the shoot apical meristem PIN1 specifically is the most highly expressed PIN and mutants of PIN1 have a lack of organ phenotype. But in other tissues other PINs play a larger role. PIN proteins are often found localized to predominantly one side of the cell, which leads to polar auxin transport. The

Figure 2.1: Indole-3-acetic acid (IAA) is a weak acid and is almost completely deprotonated in the neutral pH of the cytoplasm, preventing the charged conjugate base from diffusing through the lipid bilayer membrane. PIN1 transports IAA to the apoplasm where the pH is more acidic around 5.5. A significant portion of the IAA population becomes associated with H(+) ions, neutralizing the molecules' charge and allowing them to diffuse through the membrane into the cytoplasm of either a neighboring cell or back into the originating cell. Auxin importers like AUX1 also transport IAA across the membrane, where it becomes deprotonated and trapped again.

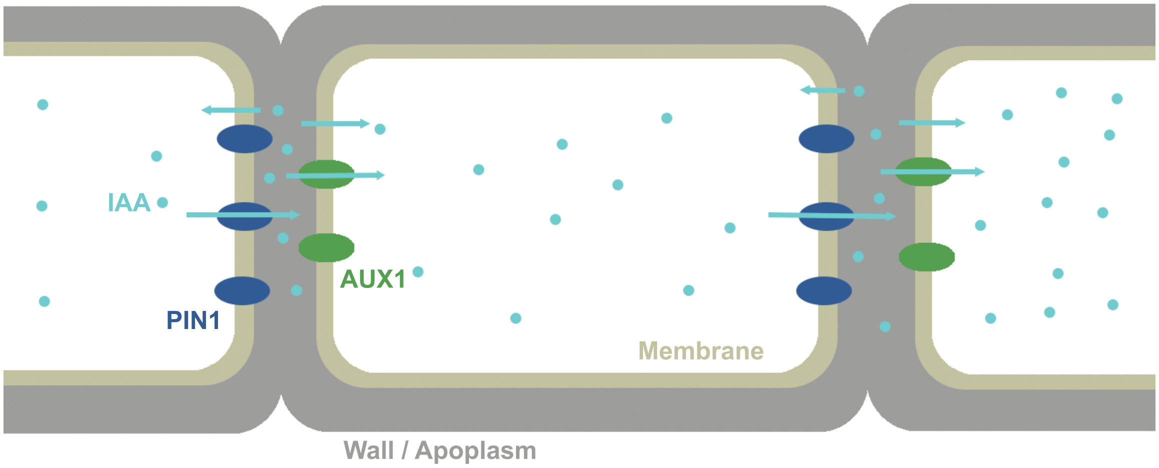

pattern of polarization of these PINs is often found to be correlated with local auxin concentration, as reported by DR5 expression[31]. The mechanism that controls this polarization involves many known components including cytoskeletal elements, vesicles, and ion signals[32, 33, 34, 35].

Currently, the most well accepted model for how PIN is localized involves PIN being secreted (to the plasma membrane, not into the apoplasm) equally to all sides of the cell. Subsequent endocytosis is polar and recycles PIN from only the sides of the cell where PIN will not be present[36]. A key component of this recycling mechanism is the endosome-localized GTPase GNOM, which is critical for endosome structure and required for proper PIN polarization[37, 38]. But there are also GNOM independent recyling pathways. For example, plasma-membrane-localized PINs can be phosphorylated by kinases, which label them for GNOM independent recycling[38, 39].

In addition to controlling the polarization of PIN proteins, recycling of PIN back to the lytic vacuole also regulates the overall concentration of PIN found in the membrane[40, 41, 42]. Part of this regulatory mechanism depends on auxin rather than proteins. Increased or decreased concentrations of indole-3-acetic acid can inhibit or promote the endosome-dependent recycling of PIN but how the concentration is sensed in this case is still unknown[40, 43, 44]. Additionally, through a mechanism unrelated to the processes just described, MAB4 is known to regulate overall PIN concentration at the plasma membrane and possibly have some role in PIN polar localization as well[45, 46, 47, 48]. Although this particular pathway is still largely unmapped, it is speculated that PINs are ubiquinated and the ubiquitin signal controls the movement of PINs through the secretory and endocytosis pathways[40, 49, 50].

Even though secretion and recycling are largely responsible for polar localization of PINs, the mechanism by which the cell "decides" which direction to polarize is not well known. There has long been speculation that mechanical forces are at least partially involved in morphogenesis in plants[51, 52]. Recent work has determined that both ablation and osmotic stress can cause PIN1 to polarize[53, 54]. In the case of cell ablation, PIN1 localized to the side the cell experiencing the most mechanical stress. This presents an intriguing potential mechanism for local accumulation of auxin. If increased auxin concentration leads to increased expansion, this expansion would put mechanical stress on the walls of neighboring cells. These cells would sense (through a yet to be discovered mechanism) one wall under more stress than the others and polarize PIN to that side of the cell, leading to polar auxin transport towards the neighbor with the highest auxin concentration (since that neighbor would generate the most mechanical stress).

It should be noted that most of this work has been done in roots and the exact proteins may vary in other tissues. Also, in the models used in this study, no mechanism is assumed for connecting mechanical forces to PIN localization.

2.1.3 Auxin Receptors and Signal Propagation

Auxin perception is mediated by a couple of independent signaling pathways. By far, the most well studied and well understood of these pathways involves the TIR1 receptor family and the transcriptional activators and repressors in the Aux/IAA, ARF, and TPL families.

Aux/IAA, ARF, and TPL proteins form a complex with DNA often within the promoter regions of auxin-responsive genes, and act as repressors[55, 56]. In the presence of auxin, TIR1/AFB and Aux/IAA bind together and additionally promote the ubiquitination and subsequent proteosome-mediated degradation of Aux/IAAs in this complex[57, 58]. It should be noted that each of these families has many members and the individuals form many distinct complexes with varying sensitivities to auxin and affinities for different DNA sequences[59]. The sensitivity to auxin is primarily determined by the Aux/IAA individuals while the DNA binding affinity is determined by both the TIR1 and Aux/IAA individuals.

Individual proteins of the ARF family of transcriptional regulators can act either as activators or repressors[60]. They can act on their own in the absence of other auxin-related factors or can work in tandem with Aux/IAA and TPL. The ARF activators usually form complexes with Aux/IAA while the ARF repressors tend to work independently of other factors[61]. Since the ARFs are not auxin receptors themselves, ARF repressors working independently of Aux/IAA are probably activated completely independently of auxin. This, in theory, provides a mechanism for other currently unknown processes to tune the auxin sensitivity of a particular promoter.

While this pathway is vast and complex, some of the details are important to the research I present here because of my use of the synthetic auxin-responsive promoter DR5. DR5 has long been used as a reporter of auxin signaling because it is activated downstream of the Aux/IAA/TIR1/ARF/TPL complex regardless of which exact individuals from those families were involved. But it is now becoming apparent that the DR5 promoter is probably only good for measuring the ratio of ARF activators and ARF repressors in a given cell. Recently, a new auxin reporter was created (DII-Venus) by fusing the auxin-interacting portion of an Aux/IAA protein with the Venus fluorescent protein[62]. This fusion protein is driven with a constituitive promoter and is on in all cells. When auxin is present, the Aux/IAA domain is ubiquitinated and degraded, destroying the Venus protein as well. This reporter system, while a more direct measurement of local auxin, does not necessarily measure the auxin-dependent transcriptional state[59, 62, 61]. But it does provide more information about the state of auxin distribution within a tissue.

Another auxin signaling pathway is the ABP1 pathway. ABP1 is a protein that can bind to and respond to primarily IAA[63]. It is found in both the apoplasm (outside of the cell) and in the lumen of the endoplasmic reticulum, although it is currently not known if ABP1 is inactive in one of these locations.

ABP1 is known to be involved in auxin-dependent regulation of cell cycle[64, 65]. It seems to be active in many different tissues including the root and shoot both during embryogenesis and later plant development[66, 67, 68]. The exact mechanism is not known but it is known to operate completely independent of the TIR1/Aux/IAA/ARF system just discussed[44, 69]. In fact, it may primarily act through post-transcriptional mechanisms[44, 69]. For example, ABP1 when bound to auxin can interfere with endocytosis, which subsequently can effect the polarization of PIN protein[43, 44], as discussed in section 2.1.2. This function is probably mediated through ROP GTPases[69]. But even though we have evidence of ABP1 acting through post-transcriptional mechanisms, it is known that it can in some instances affect the transcription of auxin responsive genes[68, 70]. But since BP1 is located in the apoplasm and ER while the known auxin-responsive transcription factors are in the nucleus, how this signal is propagated is currently unknown[70].

There is a third, less studied pathway that operates independent of the ABP1 and TIR1 pathways. This pathway involves a protein phosphatase called Indole-3-Butyric-Acid Response 5 (IBR5) which, despite the name, is able to respond to all known forms of auxin, not just IBA. Plants carrying mutations in IBR5 are smaller and have fewer lateral roots just like many mutants defective in auxin synthesis or signaling[71]. Unlike the case with TIR1 signaling, activation of the IBR5 pathway does not cause the deactivation of Aux/IAA proteins, so the transcriptional response is *probably* independent of ARF-mediated activation. But at this time the downstream targets are not known.

Regardless of the exact mechanism through which auxin is sensed, the end result is the activation of certain transcription factors involved in differentiation. This typically happens in local regions of high auxin accumulation.

2.1.4 Auxin Maxima

The current model of how organs initiate in Arabidopsis says that auxin accumulates in small regions composed of a few cells and that "maxima" of auxin leads to organ initiation. Multiple lines of evidence show that auxin is a major signal involved with the initiation of organ differentiation in a variety of Arabidopsis tissues and is both necessary and sufficient for the initiation process.

- Applying exogenous auxin to the surface of a wild type meristem causes the formation of organ primordia[72].
- Mutations in genes of auxin transporters lead to plants lacking some organs[73].
- Observations of the auxin transporter PIN1[31] suggest that auxin is being transported towards the locations where new flower primordia eventually form[74, 75, 76, 77].
- The synthetic auxin transcriptional reporter DR5 is highly expressed in areas of the shoot apical meristem where PIN1 appears to be transporting auxin towards and in the early flower primordia tissue[74, 76, 78].
- Observations of the recently developed DII-Venus reporter (see section 2.1.3) has corroborated the DR5 observations, further confirming the presence of auxin maxima at early floral organ sites.

Most of this evidence referenced is from work done in the shoot apical meristem. As a result, much of our current understanding of auxin maxima originated from shoot or root meristem observations. But some of the core concepts of auxin transport and maxima have been transferred to other tissues and have lead to a better understanding of their hormone-driven development. In the following sections I will cover auxin maxima in shoot meristems, roots, leaves, and the shoot vasculature.

2.1.5 Meristem Patterning

The Arabidopsis shoot apical meristem (SAM) is a dome shaped structure at the top (apical end) of the shoot that gives rise to all of the above-ground tissue. At the center of this structure is a group of slow-growing cells called the "central zone", commonly thought to be the stem cells of the SAM. Even though the SAM is actively growing the size of the central zone is maintained through a complex signlaing mechanism extensively reviewed by Jennifer Fletcher[79]. Outside of this circular region, cells differentiate and create the leaves or flowers which grow outward from the edge of the shoot in regular and predictable arrangements.

The arrangement of these organs around the SAM is a process called phyllotaxis. The pattern is composed of two components: the angles between successive organs called the divergence angle and the time between subsequent organs called the plastochron. The particular pattern displayed is often constant within a species but will sometimes change patterns when the meristem switches from vegetative to reproductive mode (switches from producing leaves to producing flowers). For example, both the leaves and flowers within Arabidopsis form a spiral pattern where each flower or leaf is positioned approximately 137° from the previous leaf or flower. Other patterns that can be formed by phyllotaxis are

- *alternate* - each successive organ is positioned 180° from the previous organ
- *opposite* - two organs form simultaneously 180° from each other
- *decussate* - like opposite but each 180° pair of organs rotates 90° relative to the previous pair
- *whorl* - similar to spiral but multiple organs are formed simultaneously creating multiple spirals.

The phyllotaxis pattern is the result of auxin patterning. Auxin accumulates in small regions around the periphery of the meristem outside of the central zone as a result of the complex processes described in sections 2.1.1 through 2.1.4. Regions of high auxin concentration begin differentiation into an organ and deplete the immediate surrounding tissue of auxin, preventing organs from forming in that region. Looking at the SAM from the top down and thinking of it as a flat, circular, 2D surface, each organ forms at a location at a particular angle with respect to the previous organ pivoting around the SAM apex. This angle is the phyllotaxis angle.

Since patterning of this tissue as we currently understand is dependent on the synthesis, polar transport, and signaling of auxin, perturbations to various components of this system should lead to disturbances in the wild-type phyllotaxis pattern. But mutations in the genes involved in synthesis, transport, and signaling of auxin don't lead to noticeable phyllotaxis defects, such as switching from a spiral to an alternate pattern. In order to understand how perturbations to the underlying mechanisms affect phyllotaxis in the SAM, precise measurements will be needed.

2.1.6 Root Patterning

The roots of Arabidopsis form branches, called lateral roots, similar to the above-ground branches and alternate the site of initiation 180° from the previous lateral root. These lateral root structures are important for gathering water and nutrients from the soil as they greatly increase the surface area. As the primary root grows downward some pericycle cells in the root become "founder cells" which eventually give rise to the lateral root [80]. All pericycle cells can divide when the concentration of auxin in that region becomes elevated with respect to neighbouring regions[81] but only some of these pericycle cell divisions lead to lateral root formation [82].

While we have known that auxin is required for lateral root formation since the discovery of the *alf3* and *alf4* mutation[83], the exact mechanism of the pattern has alluded us until recently. But there have been a number of observations over the past decade that gave us clues to the mechanism.

1. Mechanical stimulation of the root induces lateral root initiation [84]. When the root is forcefully bent a new lateral root often initiates on the outer edge of the bend, similar to how they usually initiate on the outer edge of the waves. Even in *arf7/arf19* double mutants this phenomenon is still observed which suggests the bending activates a pathway downstream of auxin-mediated transcriptional activation. These observations hint at a mechano-sensory component to the phenomenon but to date no one has discovered a mechanical force sensor in Arabidopsis.

2. The spacing of lateral root initiation is influenced by gravity. It has been observed that the lateral roots often form on the outside edge of an oscillating primary root. For example, Lucas et. al. showed through a combination of experiments and modeling that lateral root initiation and root gravitropism are co-regulated and that the gravitropism response has some influence on the lateral root patterning[85]. It it still unclear how much gravitropism influences lateral root initiation since the phenomenon is dependent on a particular geometry (oscillations along the length of the primary root) which is created independent of gravity. The phenomenon could probably be explained through a mechanism parallel to gravity sensing.

3. Auxin influences the space between the founder cells (and therefore the lateral roots) by priming the underlying xylem cells in the basal meristem by accumulating in certain protoxylem cells[86].

Given these observations, it is clear that Arabidopsis roots respond to a variety of inputs. Considering that roots must deliver a wide variety of nutrients, find water at varying depths, and avoid obstacles and traverse heterogeneous soils it is not surprising that they can respond to a variety of different stimuli. But it is still unclear if there is a master regulator of lateral root initiation that is influenced by these different inputs or if there are multiple, independent pathways that lead to lateral root initiation.

2.1.7 Auxin-Driven Patterning in other Tissues

It is sometimes assumed that the patterning of the vegetative (leaf producing) shoot apical meristem works similarly to the reproductive (flower producing) meristem with auxin being directed to locations around the periphery of the meristem. In the reproductive SAM, PIN1 mutants do not produce flowers. But in the vegetative SAM, PIN1 mutants still produce leaves[87]. So the assumption that both meristems work exactly the same is obviously flawed. We know that PIN1 is present in the Arabidopsis vegetative meristem[75] and that application of exogenous auxin to *tomato* vegetative meristem causes leaf primordia formation[72]. So assuming that auxin is still playing a similar role in the vegetative meristem is probably safe. But more work will be needed to determine how the vegetative SAM is able to produce leaves without PIN1. In particular, observing fluorescent proteins fused to other PIN proteins would probably yield interesting results.

Beneath the shoot meristem, vascular bundles form that are composed of xylem and phloem elements that transport water and nutrients throughout the plant. These bundles form in a circular pattern with regular spacing[88]. The auxin transporter PIN1 is known to be expressed in xylem and procambium cells, primarily polarized to the basal side of the cells but often laterally as well[24]. Inhibition of PIN1, either through genetic mutation or chemical inhibition, leads to an over-proliferation of xylem cells which spread out around the vascular ring more than in wild type. Additionally, recent work has shown that in brassinosteriod mutants, alterations to the size of the cells in the vascular ring lead to changes in the number of vascular bundles[89]. The authors speculate that an auxin patterning mechanism similar to SAM is at work in the vascular ring.

Leaf edge serrations are also thought to develop with a similar mechanism to the SAM. Leaf primordia arise from founder cells in the periphery of the vegetative SAM at sites of high auxin concentration. Development of a primordium to a mature leaf happens in two distinct stages. During "primary morphogenesis" the primodium grows through a combination of cell divisions and expansion. During this stage the leaf gets its basic shape and the vascular pattern forms and links up with the shoot vasculature. Then during "secondary morphogenesis" the leaf grows primarily through cell expansion until it reaches its final size[90, 91, 92]. It is during the primary morphogenesis stage where serrations at the edges of leaves are formed[93]. Polarized PIN1 transports auxin to sites around the leaf edge where it accumulates as evidenced by observations of pPIN1::PIN1-GFP and pDR5::GFP fluorescent reporters during leaf development[94, 95]. At the site of auxin maxima two things happen. First, PIN1 polarization flips and directs auxin inward through the leaf marking the location of vein formation[96]. Second, the cells in that regions divide and expand more than the cells in the auxin minima, ultimately leading to an outgrowth on the edge of the leaf called a serration. Since this process involves many of the same genes as the analogous process for primordia formation in the SAM, the spacing of the serrations is often thought work through the same mechanism.

Since the processes for auxin patterning just described involve many components and operate in tissues with complex geometry, efforts to understand them through back of the envelope calculations prove difficult. In order to further understand them, computer models than can solve many biochemical differential equations simultaneously are needed.

2.1.8 Modeling

As described in section 2.1.2, auxin has been long thought to influence its own distribution[97]. Given that we currently do not have a complete molecular understanding of the mechanism by which auxin is sensed and PIN proteins are localized, our current models for explaining auxin's self-influenced patterning assume two very different underlying phenomena. These models can be grouped into two paradigms: flux-based models and concentration-based models. All of these models have been created in a top-down approach where hypothetical mechanisms are devised to explain the observed patterns. And despite assuming completely different underlying mechanisms, both theoretical model paradigms are capable of producing patterns that look similar to the distribution of auxin in live tissue, as measured via DR5 expression.

The flux models are based on Sachs' canalisation hypothesis[97] which states that cells experiencing flux of a molecule in a certain direction will increase their capacity to transport the molecule in that direction and is based on the observation that during vein formation auxin transport channels become gradually more distinct. In early models, the degree of polar auxin transport is represented by a membrane permeability coefficient[98, 99]. After the discovery of PIN proteins, later models represented the polar auxin transport by coefficients representing concentration of PIN1 on the membranes, degree of polarization, and transport rates[100, 101, 102, 103, 104]. Primarily, these models have been used to understand the process of leaf vein formation. Small differences in initial PIN concentration or polarization are able to self-amplify and create patterns similar to those seen in leaf veins.

Concentration-based models[105, 106, 107, 108] were formulated after the discovery of PIN proteins and therefore all explicitly model membrane PIN levels. In these models, PIN levels increase on the membrane facing the neighbouring cell with the highest auxin level, i.e., up-the-gradient. This proposed feedback mechanism was inspired by observations in the shoot apex, where PINs in the epidermal layer orient toward local auxin maxima that develop into organ primordia [75, 78]. Concentration-based models are sufficient to obtain phyllotaxis-like patterns by amplifying small local increases in auxin into distinct maxima while simultaneously depleting neighbouring cells, resulting in the occurrence of new maxima at fixed distances from older maxima.

More recently, there has been a trend to make concentration based models that can behave like both flux-based and concentration-based models depending on the topology of the tissue and starting conditions[109, 108, 104]. This is the result of thinking that there is a single common mechanism underlying all auxin pattering phenomena. If a single mechanism *is* responsible for all auxin patterning in all tissues then a single model should be able to explain all of these observations. Additionally, even more complex models have been proposed that consider more than just cell geometry, auxin, and PIN1. As mentioned in section 2.1.2, there is evidence that mechanical forces are at play in the PIN1-auxin feedback loop. Based on these observations, models were made that incorporate stress-responsive alignment of microtubules, seeking to understand how mechanical stress is involved in phyllotaxis patterning[110]. Unfortunately, due to the nature of the math involved in calculating stress in an arbitrarily shaped tissue, the finite element method is required in this model which makes it difficult to incorporate other dynamic phenomena like cell division. Thus, while the model adequately explains how a stress-auxin-PIN1 feedback loop would work it cannot demonstrate the process in an actively growing phyllotaxis model. Although, it may be possible in the future to use a remeshed particle method to adequately model mechanical stress, auxin transport, and cell expansion and division in a single model[111].

In this work I seek to understand how universal our current understanding of auxin patterning is within the context of different *Arabidopsis* tissues, specifically SAM, root, leaf, and shoot vascular tissues. I will start by probing the robustness of our current phylloaxis model and determine which parameters alter the phyllotaxis pattern most dramatically. Using these computational observations, I will seek mutants that have defects in the parameters predicted by the model to have a large effect on phyllotaxis. Using these mutants I will observe auxin distribution in different tissues and determine if there are perturbations to the auxin distribution similar to those predicted by the model.

2.2 Methods

2.2.1 Plants and Growth Conditions

Seeds from the genetic backgrounds Col-0 (wild type), L-er (wild type), *msc3* (a.k.a. sqn-3), Wa-1 and *cycd3;1-3* were used. The wild type lines Col-0 and L-er were acquired from lab stocks. *msc3* seeds were a gift from Dr. Hirokazu Tsukaya at the University of Tokyo. *msc3* was originally identified in a T-DNA insertion library made with Col-0 plants, so *msc3* seeds were back crossed four generations before use. Wa-1 was acquired from the Arabidopsis Biological Resource Center, germplasm ID CS1586. *cycd3;1-3* seeds were acquired from Adrienne Roeder, who made the line using 2 EMS mutants and a T-DNA mutant (*cycd3;1*,*cycd3;2* and *cycd3;3*). This triple mutant was from both Col-0 and L-er backgrounds so it was back-crossed to Col-0 three generations before use. Triple mutant plants were initially identified by their large size and thick stems. Plants with the correct characteristics were self-crossed and lines that showed no segregation were confirmed to have the correct homozygous mutations and insertions using PCR and sequencing.

2.2.1.1 Growing on Plates

When selecting seeds on plates, seeds were sterilized with 70% ethanol and added to agar plates. The agar plates were made with the following composition:

- 1% PhytoAgar
- 4.3g/L Murashige and Skoog Basal Salt Mixture
- 1mL 1000x concentrated Murashige and Skoog Vitamin Solution
- 30g/L sucrose
- 50ug/mL kanamycin monosulfate.
- 1L DI water

All components except for kanamycin were mixed in a 2L flask and then adjusted to a pH of 5.7 while mixing with a stir bar. The solution was autoclaved for 30min. When the temperature reached 60°C the kanamycin was added from a stock ethanol solution. Plates were poured in a sterile environment.

The sterilized seeds were dried on sterile filter paper and then applied to the MS agar plates. Plates were taped closed with filter tape and stored at 4°C. After a three day vernalization at 4°C, seeds were germinated under constant light at room temperature. 10 days after germination, healthy looking plants were transferred to soil.

Materials for Growing on Plates

- Murashige and Skoog Basal Medium (Sigma Aldrich, #M9274)
- Murashige and Skoog Vitamin Solution (Sigma Aldrich, #M3900)
- Sucrose
- Phytoagar (Spectrum Chemical, #40100072)
- Kanamycin (Sigma Aldrich, #60615)
- Deionized water
- Western incubation box 2.875" x 2.00" x 1.25" (Crystalgen, #G755)
- Filter tape, nonwoven, pressure sensitive (Carolina, #199708)
- 1M KOH
- Aluminum foil
- 25ml Serological pipet (USA Scientific, #1072-5410)

2.2.1.2 Growing in Soil

When growing in soil, pots of soil were made using the following composition:

- 2 parts Sunshine Mix
- 2 parts SuperSoil Potting Soil
- 1 parts Vermiculite
- 1 parts Perlite
- 0.02 parts Marathon insecticide

Pots were arranged in flats of 12 pots and stored at 4°C for three days before transferring to a growth chamber with 24h illumination. Flats were given 1cm of water every two days.

Materials for Growing in Soil

- High wall petri dishes (Electron Microscopy Sciences, #64332)
- Sunshine Mix (McConkey Co, #SUNSM2)
- SuperSoil Potting Soil (SMG Growing Media)
- Vermiculite #2 Coarse (McConkey Co, #TRWVMIC26)
- Perlite (McConkey Co, #TRWPERL6)
- Marathon Insecticide 1% (OHP Inc, EPA #432-1329-59807)

2.2.2 Fluorescent Lines

A pDR5::2xGFP-N7 fluorescent reporter construct was built using standard Gateway cloning techniques. That construct was transferred to the pMOA33 plasmid, a binary plasmid carrying a kanamycin resistance cassette. In E. coli this plasmid was selected on LB agar using spectinomycin. This E. coli line was mated with an Agrobacteria tumefaciens line carrying the other half of the binary plasmid system and a helper E. coli line. The resulting Agrobacteria tumefaciens line was selected at 27°C on LB plates containing rifamycin, gentamycin, and spectinomycin as the Agrobacteria tumefaciens line contains a rifamycin cassette in its chromosome and a gentamycin cassette on its plasmid.

All Arabidopsis lines previously mentioned in section 2.2.1 were transformed using this pDR5::2xGFP-N7 line using the floral dip method. To transform these plants, seeds were first grown on soil, four plants to a pot, under continuous light. Primary shoots were clipped to encourage growth of multiple secondary shoots. Plants were ready to dip eight days after clipping. A large liquid culture of the Agrobacteria tumefaciens line was grown with LB rifamycin, spectinamycin, and gentamycin at 28°C. Cells were grown until mid log phase. The culture was spun down at 8,000rcf and then resuspended to an OD600 of 0.8 in a 5% aqueous sucrose solution. Before dipping, Silwet L-77 was added to the bacteria sucrose solution to a concentration of 500uL/L or 0.05% and mixed well. Plants were dipped in the bacteria solution for 30 seconds and then transferred to a covered flat with high humidity for 24 hours. These flats were stored at 16°C for four days and then transferred back to the original growth room, uncovered and exposed to continuous light.

Transformed seeds were grown on MS kanamycin plates as previously described. After roots emerged, plates were inverted and viewed under epifluorescent illumination at 100X magnification (10X 0.24NA objective, 10X eyepieces). Roots with high expression of GFP in the roots were marked and were later transferred to soil. These plants were self crossed and homozygous lines were determined after the third generation. Of these homozygous lines, meristems were dissected and observed with laser scanning confocal microscopy. Lines that had visible GFP expression in the meristem (in addition to expression in the roots) were selected for further experiments.

2.2.3 Meristem Experiments

Plants containing the pDR5::2xGFP-N7 fluorescent reporter as described in section 2.2.2 were germinated on MS and kanamycin agar plates and then transferred to soil as previously described in section 2.2.1.2. These plants were grown under continuous light until the shoots entered the reproductive phase and bolted. Flowers were removed with sharp forceps under a dissecting microscope. The meristem and approximately 5mm of stem were removed using forceps and placed in a glass slide. The slide was refrigerated for 15 minutes. This slows endocytosis, which would increase the background noise while imaging FM4-64.

High wall petri dishes were prepared with 1% phytoagar made with DI water. A 1mL solution of 5ug/mL FM4-64 in DI water was prepared from a 200ug/mL stock solution of FM4-64.

After the meristem tissue sat at 4°C for 15 minutes, 50uL of the FM4-64 solution was placed on each meristem using a 200uL pipette. The glass slide containing the meristems was placed back in the refrigerator at 4°C for another 15 minutes. Small holes were poked in the agar in the petri dishes. The meristems were removed from the slide and the drop of FM4-64 solution was removed with a Kimwipe. The Meristems were then stuck into the holes in the agar facing upward so the stems protruded into the holes, holding the meristems firmly in place. DI water was added to the petri dishes to a height 1cm above the top of the meristems.

Meristems in agar were imaged using a Zeiss LSM 510 laser scanning confocal microscope with a 63x 0.95NA Achroplan water dipping objective. The sample was excited using a single 488nm laser through a 488nm dichroic mirror which can excite both FM4-64 and GFP. A 500-525nm bandpass filter was used to capture light from GFP and a 650nm longpass filter was used to capture light from FM4-64 simultaneously.

Images from this procedure were processed using the technique described below in section 2.2.11. Meshes generated in MorphoGraphX were analysed to find the locations of fluorescent nuclei and the distance between those clusters of nuclei.

2.2.4 Root Experiments

Plants containing the pDR5::2xGFP-N7 fluorescent reporter as described in section 2.2.1 were germinated on MS and kanamycin agar plates as previously described in section 2.2.1.1. Five days after germination, healthy looking plants were transferred to glass slides. Slides were previously prepared with two pieces of 28 gauge steel wire glued to the slide oriented parallel and spaced apart less than the width of a cover slip to prevent the cover slip from crushing the roots. Each slide contained approximately five plants next to each other oriented in the same direction to make finding root tips easy under magnification. The slide was refrigerated for 15 minutes. This slows endocytosis, which would increase the background noise while imaging FM4-64.

A 1mL solution of 5ug/mL FM4-64 in DI water was prepared from a 200ug/mL stock solution of FM4-64. After the plants sat at 4°C for 15 minutes, 20uL of the FM4-64 solution was placed on each root tip using a 200uL pipette. The glass slide containing the roots was placed back in the refrigerator at 4°C for another 15 minutes. After removing the slides from the refrigerator, the drop of FM4-64 solution was soaked up with a Kimwipe. 75uL of DI water was added to the slide and a cover slip was added, crushing the cotyledons but leaving the roots in good condition. The cover slip was quickly tacked down with two drops of quick drying clear nail polish.

The roots were imaged using a Zeiss LSM 510 laser scanning confocal microscope with a 63x 0.95NA Achroplan water dipping objective. The sample was excited using a single 488nm laser through a 488nm dichroic mirror which can excite both FM4-64 and GFP. A 500-525nm bandpass filter was used to capture light from GFP and a 650nm longpass filter was used to capture light from FM4-64 simultaneously.

In order to capture images up the length of the root, many overlapping images were taken of each sample starting at the root tip and travelling approximately 500um up the root apically. Images were saved as LSM files then processed in the Fiji software suite[112]. The many images from each sample were stitched together into a single z-stack. In order to quantify the distance between DR5 expressing cells in the root, the number of cells between these points of interest were counted manually while the absolute distance was quantified using Fiji's built-in measuring tool.

2.2.5 Vascular Experiments

All the fluorescent lines previously generated in section 2.2.2 were used in the vascular experiments. Plants were grown on soil as described in section 2.2.1.2 until the plants were mature. Samples of each plant were taken by cutting a 2mm tall section of shoot using a razor blade. The samples were taken between the first and second carpel starting from the basal end of the shoot. These sections were fixed with formaldehyde, embedded with paraffin, stained and imaged.

Materials Used

- Paraformaldehyde (Sigma Aldrich #P6148)
- 1x Phosphate Buffered Saline solution, pH 7.4 (Life Technologies, #10010-023)
- NaOH, pelletized (Sigma Aldrich #221465)
- H_2HSO_4 (Sigma Aldrich #320501)
- Triton X-100 (Sigma Aldrich #X100)
- Ethanol, no denatured
- HistoClear (National Diagnostics #HS-200)
- DI water
- Paraplast Plus (Sigma Aldrich #P3683)
- Petri dishes
- Large plastic weigh boats
- Toluidine Blue O (Sigma Aldrich #T3260)
- Razor blades
- Glass scintillation vials (Wheaton Scientific #986746)

Equipment Used

- Leica Microtome
- Laboratory oven
- Heated water bath
- Slide Warmer

- Vacuum Chamber
- Glass jars
- Glass slide holders
- Forceps
- Metal spatula

2.2.6 Fixing

Fresh 4% paraformaldehyde (PFA) fixative was prepared. For 500 ml, 400 ml 1x PBS (130 mM NaCl, 7 mM Na_2HPO_4, 3 mM NaH_2PO_4 pH7.4) was warmed to 60°C and two pellets of NaOH were dissolved. In a fume hood, 20 g of paraformaldehyde was added and mixed thoroughly until dissolved. The solution was placed on ice and when cooled, the pH was adjusted to 7.2 with H_2HSO_4 (1-2 drops for 100ml). The volume was adjusted to 500 mL with 1x PBS.

Samples were harvested and placed immediately in 15 mL fresh PFA fixative on ice in glass scintillation vials. Large volumes of fixative were used; usually 20 volumes of fixative to one volume of tissue.

A vacuum (~500 mm Hg) was applied to the samples while on ice. The vacuum was held for 20 minutes while bubbles were released from the sample. The vacuum was slowly released and the samples were then transferred to a new solution of fixative to insure that the tissue remained in the right concentration of fixative. This vacuum step is applied repeatedly until the samples sink to the bottom of the jar of fixative, indicating that all the air bubbles have been released. When samples were not easily penetrated by the fixative, 0.1% Triton X-100 is added to the fixative and the procedure was repeated. Finally, the samples were once more transferred to new fixative and stored at 4°C overnight.

2.2.7 Embedding

A 1xPBS solution and a series of ethanol solutions were pre-cooled to 4°C. The samples were removed from the fixative solution and rinsed in 1xPBS on ice for 30 minutes. The samples were removed and then put in a fresh 1xPBS solution on ice for another 30 minutes.

The samples were removed from the 1xPBS solution and dehydrated with the following series of ethanol solutions.

- 10% ethanol 30 minutes
- 30% ethanol 30 minutes
- 50% ethanol 60 minutes
- 70% ethanol 60 minutes
- 85% ethanol 60 minutes
- 95% ethanol 60 minutes
- 100% ethanol 60 minutes
- 100% ethanol 60 minutes
- 100% ethanol 60 minutes

After the samples were taken through this entire series they were placed in a solution of 0.1% eosine in 100% ethanol and sat overnight at 4°C. Adding eosine to the samples made it easier to find them later once embedded in the semi-transparent paraffin.

Three ethanol/histoclear mixtures (3:1 v/v, 1:1 v/v, and 1:3 v/v) were prepared at room temperature in glass jars as well as a jar of 100% histoclear. The vials containing the samples in ethanol and eosine were decanted and then the following series of mixtures was added to the vials, decanting in between each one.

- ethanol/histoclear (3:1 v/v) 90 minutes
- ethanol/histoclear (3:1 v/v) 90 minutes
- ethanol/histoclear (3:1 v/v) 90 minutes
- 100% histoclear 90 minutes
- 100% histoclear 90 minutes
- 100% histoclear 90 minutes

Paraplast chips were placed in a beaker and heated to 60°C in a laboratory oven to melt the paraffin. When not being used the beaker of paraffin was stored at 60°C. The samples is histoclear were poured into large plastic weigh boats. Molten paraffin was added to the weigh boats and then the weigh boat was placed in the 60°C for one hour. After an hour, more molten paraffin was poured into each weigh boat. This was repeated every hour for eight hours. Then the histoclear/paraffin mixture was decanted from the weigh boat, leaving the samples behind with a minimal amount of histoclear/paraffin. Fresh molten 100% paraffin was added to the weigh boats. The weigh boats were left overnight at 60°C.

The following day the molten paraffin was replaced with fresh paraffin every four hours, three times. The weigh boats were kept at 60°C the entire time. The following day this procedure was repeated another three times.

The following day a petri dish was filled with molten paraffin and warmed to 60°C. The samples in the weigh boat were transferred to the petri dish using a warm metal spatula. Once all the samples were in the petri dish of paraffin they were arranged to all be oriented the same direction sitting side by side. This makes it easier to cut around them later.

The petri dish was then cooled to room temperature and the paraffin hardened. The dish was left at room temperature for three hours to ensure the paraffin had hardened all the way through. Once it was completely solid a razor blade was used to cut small cubes of parafin out, each one containing a single tissue sample. The cubes were trimmed down to approximately 5mm by 5mm in size so there was a minimal amount of excess paraffin.

Each sample was then placed on a microtome pedestal. The concave surface of the pedestal was filled with molten paraffin and the sample, embedded in a cube of paraffin, was held with forceps on top of the molten paraffin while it solidified. The pedestal was then mounted on the microtome.

2.2.8 Sectioning

After a pedestal was mounted on the microtome, the blade was aligned with the sample and the pedestal was rotated so the blade would cut through the narrowest side of the block first. The microtome was set to 10um increments and then gently turned so that the sample formed a ribbon. The ribbon was floated in a 40°C water bath and then removed using a small paint brush. The ribbon was placed on a glass slide. The glass slide was then placed on a 40°C slide warmer and left to dry for one hour.

This procedure was done for each sample and then the slides were labelled with a marker.

Before removing the paraffin, the samples were stained with Toluidine Blue O. A solution of 0.05%

(w/v) Toluidine Blue O was made in 10mL of DI water. This solution was added to a glass slide jar and the slides were placed in the solution for 30 minutes. The slides were then removed and rinsed with DI water.

To remove the paraffin from the samples and slides, first a series of histoclear and ethanol baths were prepared. These liquids were placed in glass slide holders so the slides would easily stand up in the liquid, keeping part of the slide above the liquid for easy handling. The slides were taken through the following series without drying in between.

- histoclear 10 minutes
- histoclear 10 minutes
- 100% ethanol 1 minute
- 95% ethanol (5% DI water) 1 minute
- 85% ethanol (15% DI water) 1 minute
- 70% ethanol (30% DI water) 1 minute
- 50% ethanol (50% DI water) 1 minute
- 30% ethanol (70% DI water) 1 minute
- 10% ethanol (90% DI water) 1 minute
- 100% DI water 1 minute

The slides were then air dried for 30 minutes and then either stored in a slide box at 4°C or imaged immediately.

2.2.9 Imaging and Analysis

Slides were viewed on a Zeiss Axioskop with a 5x Plan-Neofluar 0.15NA objective. Bright field illumination was provied by a 10W tungstem bulb. Condenser and light source adjustments were made and then images were taken with a Zeiss Axiocam 105 Color camera.

Image files were exported as TIF files from the Zeiss ZEN software. These files were then opened in Fiji[112]. A plugin call *cell-counter* was added to Fiji to assist in numbering cells. Each cell around the base of the vascular ring was counted and numbered using the labelling tool provided by the *cell-counter* plugin.

Once the cells were done being counted, an XML file containing the label data was exported and stored with the TIF images. The number of cells was recorded for each sample.

2.2.10 Leaf Experiments

Materials Used

- FM4-64 (Life Technologies #T-3166)
- DI water
- 75mm x 25mm glass slides (Sigma Aldrich #CLS294775X50)
- 25mm x 25mm glass cover slips (Sigma Aldrich #Z692263)
- Superglue (Cyanoacrylate adhesive)

Equipment Used

- Zeiss LSM 520 laser scanning confocal microscope
- Zeiss Stemi SV11 dissecting microscope
- Forceps
- 200uL pipette

Plants containing the pDR5::2xGFP-N7 fluorescent reporter as described in section 2.2.1 were germinated on MS and kanamycin agar plates as previously described in section 2.2.1.1. Five days after germination, healthy looking plants were transferred to glass slide using forceps. A dot of Superglue was placed on the glass slide and the plant was stuck into the glue root side down with the cotyledons oriented upward. This holds the small plant in place so the meristem and leaves can be dissected easily. The cotyledons were dissected away with sharp forceps under a dissecting microscope with 10x magnification, exposing the youngest leaves. These leaves were removed by gently pushing with the forceps.

Slides were previously prepared with two pieces of 28 gauge steel wire glued to the slide oriented parallel and spaced apart less than the width of a cover slip to prevent the cover slip from crushing the leaves. Each slide contained approximately five leaves next to each other oriented in the same direction.. The slide was refrigerated for 15 minutes. This slows endocytosis, which would increase the background noise while imaging FM4-64.

A 1mL solution of 5ug/mL FM4-64 in DI water was prepared from a 200ug/mL stock solution of FM4-64. After the plants sat at 4°C for 15 minutes, 20uL of the FM4-64 solution was placed on each leaf using a 200uL pipette. The glass slide containing the leaves was placed back in the refrigerator at 4°C for another 15 minutes. After removing the slides from the refrigerator, the drop of FM4-64 solution was soaked up with a Kimwipe. 75uL of DI water was added to the slide and a cover slip was added. The cover slip was quickly tacked down with two drops of quick drying clear nail polish.

The leaves in agar were imaged using a Zeiss LSM 510 laser scanning confocal microscope with a 63x 0.95NA Achroplan water dipping objective. The sample was excited using a single 488nm laser through a 488nm dichroic mirror which can excite both FM4-64 and GFP. A 500-525nm bandpass filter was used to capture light from GFP and a 650nm longpass filter was used to capture light from FM4-64 simultaneously.

2.2.11 MorphoGraphX Image Processing

LSM images of the meristem were processed to extract the positions of the cell walls in the first layer and the locations of fluorescent nuclei. This procedure relies on the software MorphoGraphX[113] and some particular computer hardware and software.

2.2.11.1 Computer Hardware

- At least 16GB of RAM.
- Nvidia graphics card, 2GB of RAM or more recommended.

2.2.11.2 Software

- Linux operating system.
    - Ubuntu or Kubuntu will be simplest if you are not an experienced Linux user.
    - The distribution must be able to run proprietary NVIDIA graphics drivers.
- MorphoGraphX[113] (Lab of Richard Smith, Max Planck Institute for Plant Breeding Research)

  Other software that can be used in place of MorphoGraphX

  - MARS-ALT[114]
  - Bitplane Imaris
- ImageJ[115] (Fiji[112] is preferable)

The first step for importing the data into MorphoGraphX was to convert the z-stack into TIFF format. The easiest tool for this job is ImageJ or Fiji, which is a particular distribution of ImageJ with many useful plug-ins already installed. In this work Fiji was used in place of ImageJ but ImageJ can be used also. In that case a plug-in would need to be installed which allows ImageJ to read the particular z-stack format, in this case an LSM file (LSMToolbox for Zeiss LSM files, Loci_tools for Leica LIF files, Bio-formats for Nikon ND2 or Zeiss CZI files).

In order for MorphoGraphX to interpret the image file correctly the first image in the series to be the top of the meristem. When the order was reversed the data was exported as a series of individual TIFF files rather than a multi-TIFF so the order of the images could be reversed.

Before beginning the image processing, some steps were taken to taken to insure all the software was set up and our data was ready to be processed.

- ImageJ or Fiji was installed
- MorphoGraphX was installed. On Ubuntu this can be done through the built-in package manager.
- The x,y,z dimensions of the voxels from the image file metadata were retrieved.

2.2.11.3 Multiple TIFF Images

When exporting the image data from LSM files into a series of TIF images, the following procedure was used.

1. Open ImageJ or Fiji.
2. Click on *File*, then *Save As*, then *Image Sequence*.
3. Select the TIFF format and start the numbering at 0.
4. Click *OK*.
    - This will create multiple image files.
    - One file for each slice in the z-stack.

Figure 2.2: Example of an image processed in MorphoGraphX. **A.** Z-stack loaded. **B.** After surface detection. **C.** Side view after editing of surface to remove extraneous parts. **D.** Creation of coarse mesh. **E.** Image data mapped onto mesh surface. **F.** Smoothing of the data on mesh surface.

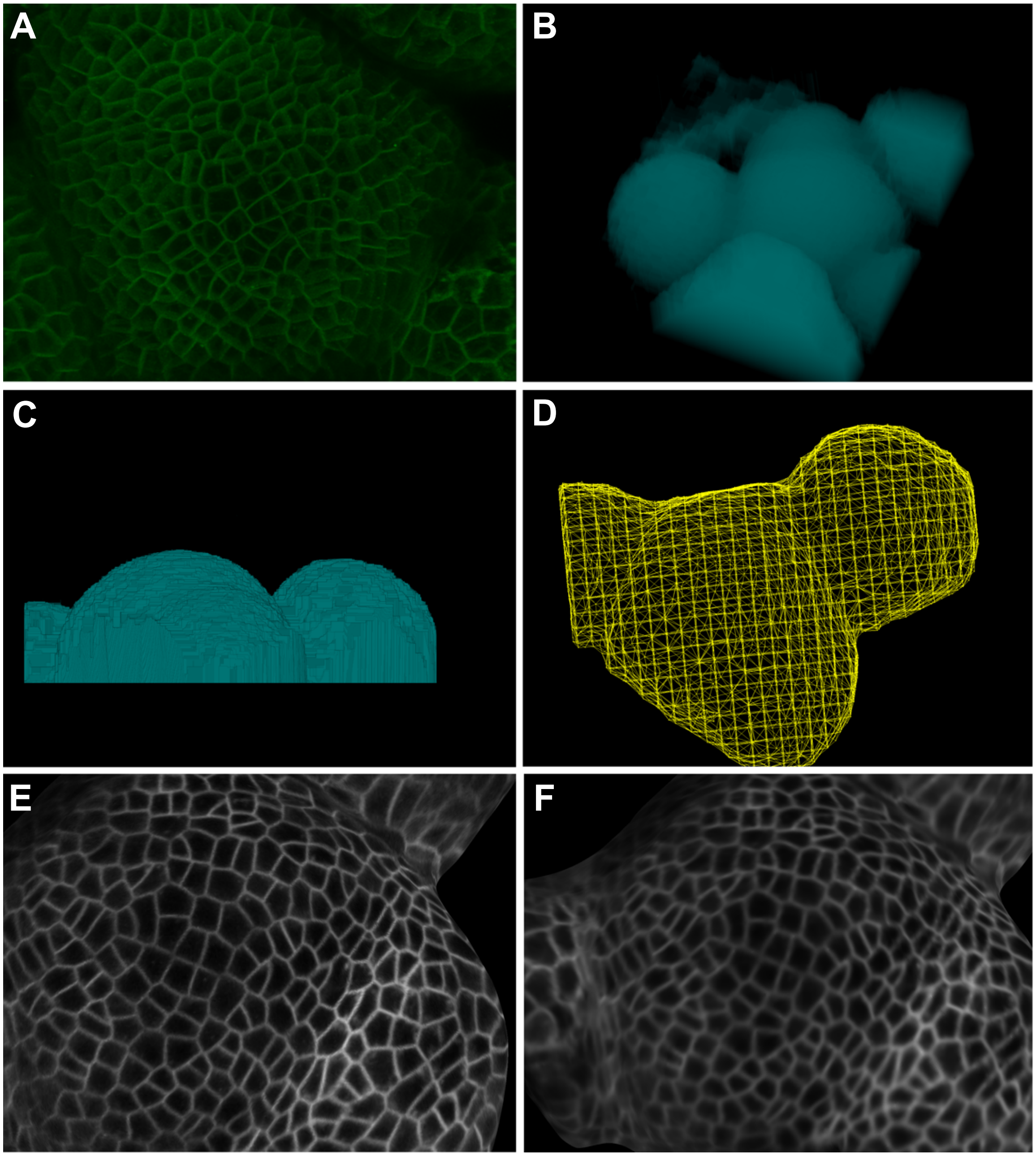

The following Bash script (OSX, Linux or Cygwin environments only) was used to reverse the numerical order of the TIF file names when needed. This assumes the files are named like "image3.tif". The second line of the script can be modified if the files are named differently. The script was copied into the same directory as the multiple TIFF files and run.

```
#!/bin/bash
image=( image*.tif )
MAX=${#image[*]}
for i in ${image[*]}
do
   num=${i:5:3} # grab the digits
   compliment=$(printf ’%03d’ $(echo $MAX-$num | bc))
   ln $i copy_of_image$compliment.tif
done
```

In order to import these TIF images into MorphoGraphX, the following procedure was used:

1. The MorphGraphX program was started.
2. In the top menu bar select *Stack* then *Stack1* then *Main* then *Image Sequence*.
3. Click *Add Files*.
4. Select all of the image files in the series.
5. Click *OK*.
6. Input the X, Y, and Z dimensions of the voxels in micrometers.
    - These data were available in the metadata associated with the original image file.
7. Click *Start* and the stack appears in the main window in a semi-transparent state as seen in Figure 2.2A.

2.2.11.4 Single TIFF Image

In order to export the data as a single multi-TIFF image, the following procedure was used:

1. Click on *File*, then *Save As*, then *Tiff*.
2. Select the TIFF format and start the numbering at 0.

  - This creates multiple image files, one for each slice in the z-stack.
  - This file is imported into MorphoGraphX.
3. Open the MorphoGraphX program.
4. Drag the TIFF file into the main window.
  - This opens a window where the X, Y, and Z dimensions of the voxels in micrometers are manually entered.
  - These data were available in the metadata associated with the original image file.
5. Click *Start* and the stack appears in the main window in a semi-transparent state as seen in Figure 2.2A.

2.2.11.5 Building the Mesh

To convert the image data into a mesh representing the surface of the meristem the following procedure was used:

1. On the right side, select the *Process* tab, then the *Stack* tab.
2. Expand the *Morphology* section.
3. Click on *Closing*.
4. Change the *X Radius*, *Y Radius*, and *Z Radius* parameters to 15.
5. Click *Go*.
6. Confirm that the cell boundaries are no longer visible and the meristem looks like a solid mass.
  - The original data is still unmodified in *Main*, *Stack1*, *Work*.
  - If the cells are still visible, increase the *Radius* parameters.
7. Click on *Edge Detect*.
8. Modify the parameters that appear towards the bottom.
  - The values for these parameters depend on the brightness and the amount of background noise in the data.
  - Start with the default values but change *Threshold* to 100000.

9. Make sure the surface looks relatively smooth as in Figure 2.2B.
    - There should be no large spikes protruding from the surface.
    - Experiment with different parameters.
10. Erase any structures that you do not want included in the mesh like flower primordia.
    - 10.1. At the top of the window select the *Pixel Edit* tool.
    - 10.2. To erase, hold *Ctrl* and *Alt* and click regions with the left mouse button.
    - 10.3. When not holding *Ctrl* and *Alt* use the mouse to move and rotate the image.
    - 10.4. Use the mouse scroll wheel to zoom in and out.
    - 10.5. Look for small extraneous bits around the meristem and erase those, too.
    - 10.6. With the opacity turned up, it should look like Figure 2.2C.
11. In the *Process* tab, click the *Mesh* tab and expand the *Creation* section.
12. Select *Marching Cubes Surface*.
13. Try the default parameters and click *Go*.
14. To view the mesh:
    - 14.1. Go to the *Main* tab, then the *Stack 1* tab.
    - 14.2. Disable *Main* and *Work*
    - 14.3. Enable *Mesh*
    - 14.4. Choose *ALL* from the *View* dropdown menu.
    - 14.5. It should look similar to Figure 2.2D.
15. Go to the *Process* tab, then the *Mesh* tab, in the *Structure* section select *Smooth Mesh* and click *Go*.
16. Select *Subdivide Mesh* and click *Go*.
17. Repeat steps 15 and 16 until there are at least 1 million vertices.
    - This number can be found at the bottom of the window.
    - More vertices will improve accuracy at the expense of memory usage.

   - At some point more vertices is no longer helpful.

18. Remove the bottom of the mesh.
    18.1. Position the meristem so you are facing it from the side. Double clicking will snap it into place.
    18.2. On the right side of the window, choose the *Select Points in Mesh* button.
    18.3. Hold hold *Ctrl* and *Alt* and use the mouse to select the entire bottom of the mesh.
    18.4. Use the *Del* key to remove the selected vertices.
19. Map the image data onto the mesh.
    19.1. Select the *Main* tab.
    19.2. Make sure the *Main* stack is selected rather than the *Working* stack.
       - This determines which data will be mapped onto the mesh.
    19.3. Select the *Process* tab.
    19.4. In the *Mesh* tab expand the *Signal* section.
    19.5. Select *Map Signal*.
    19.6. Choose 1μm for the *Min Dist* parameter and 4μm for the *Max Dist* parameter.
    19.7. Click *Go*.
    19.8. Go the the *Main* tab. Unselect *Work* and select *Mesh*. This should display the image data mapped onto the mesh.
    19.9. It should look similar to Figure 2.2E.
20. Confirm that the image data mapped on to the mesh looks good.
21. If deeper cells layers are appearing on the surface, experiment with the parameters in step 19.6.
22. Select *Smooth Mesh Signal* from the *Signal* section.
23. Click Go. This will smooth out the image data to help the segmentation algorithm produce straighter boundaries. It should look similar to Figure 2.2F.

Now the data are mapped onto the mesh. The meshed was viewed by turning off the stacks. When the image looked jagged or overly pixelated, more vertices were added to the mesh using steps 15 and 16 and then re-maped the data onto the mesh using step 19. Then the image was ready to be segmented.

The previous steps were automated using MorphGraphX's Python scripting capabilities. The following code performs the steps automatically but can't be paused to view the intermediate steps. When intermediate steps are needed to be viewed, parts of the code were commented out.

To run Python code in MorphoGraphX, the code was first saved to a text file that has the *.py* file extension. In MorphoGraphX click on the *System* tab, then select *Python*. Choose the file that contains the Python code, then click *Go*.

```
Stack.Closing(15,15,15)
Stack.Edge_Detect(100000,2,0.3,30000)
Mesh.Marching_Cubes_Surface(5,5000)
Mesh.Smooth_Mesh(1)
Mesh.Subdivide()
Mesh.Smooth_Mesh(3)
Mesh.Subdivide()
Mesh.Smooth_Mesh(1)
Mesh.Subdivide()
Mesh.Subdivide()
Mesh.Project_Signal("No",1,3,0,50000)
Mesh.Smooth_Mesh_Signal()
```

When running an older version of MorphoGraphX the stack often requires more processing before the edge detection step. In that case the following code was used.

```
Stack.Resize_Canvas("Yes","Yes",0,0,40)
Stack.Shift_Stack(0,0,20)
Stack.Average(1,1,1,1)
Stack.Closing(15,15,15)
Stack.Edge_Detect(100000,2,0.3,30000)
Mesh.Marching_Cubes_Surface(5,5000)
Mesh.Smooth_Mesh(1)
```

Figure 2.3: Segmentation of cells in MorphoGraphX. **A.** Seeds drawn on the mesh. One seed is drawn in the center of each cell. This helps the watershed segmentation algorithm correctly differentiate between different cells. **B.** After watershed segmentation. **C.** Creation of cells using 1μm line segments. **D.** Side view of the cells.

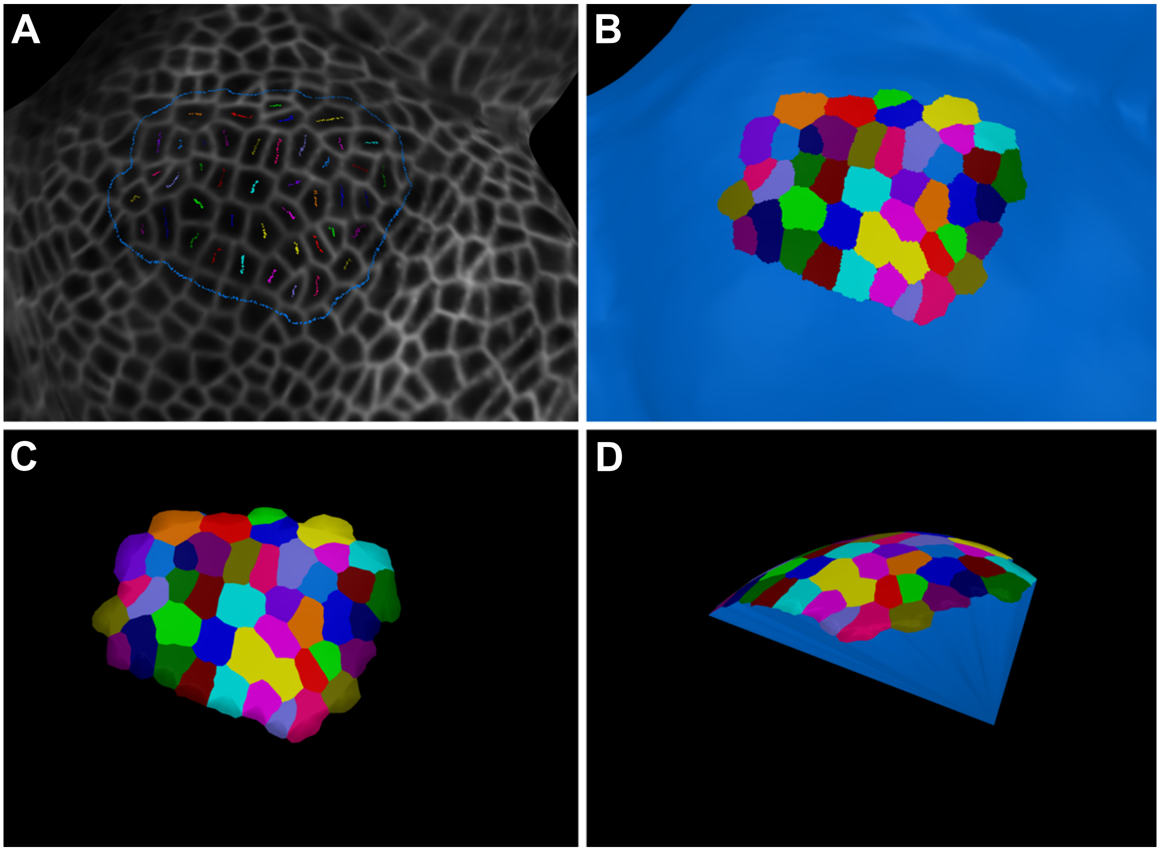

```
Mesh.Subdivide()

Mesh.Smooth_Mesh(3)

Mesh.Subdivide()

Mesh.Smooth_Mesh(1)

Mesh.Subdivide()

Mesh.Subdivide()

Mesh.Project_Signal("No",1,3,0,50000)
```

2.2.11.6 Segmenting

The following procedure was used to detect the edges of the cells in the mesh:

1. At the left side of the window, click the *Add New Seed* tool.
2. Hold hold *Ctrl* and *Alt* and use the mouse to click the interior of a cell.

3. Do this for each cell as seen in Figure 2.3A.
    - Each cell should turn a different color.
    - You can drag the mouse to color a larger portion of the cell interior.
    - This can help if the background noise is high.
    - Each time you click you are drawing with a new cell-seed.
    - If you have already picked the mouse up but want to keep drawing with the same seed, select the *Add Current Seed* tool and draw with that.
    - To revert back to making new seeds, select the *Add New Seed* tool again.
    - To erase a seed:
        (a) Click on the *Label Color* (the colored box at the top of the window). The color should disappear.
        (b) Choose the paint bucket tool.
        (c) Click on the seed that you want to erase.
    - With a new seed, draw a circle around the area you want segmented as seen in Figure 2.3A.
4. In the *Process* tab, expand the *Segmentation* section.
5. Click on *Watershed Segmentation*.
6. Use the default parameters.
7. Click *Go*.
8. Wait for the segmentation to complete.
9. The mesh should look similar to Figure 2.3B.
10. If you are satisfied with the segmentation, proceed to step 13.
11. If there are corners between the cells that are not assigned a color:
    11.1. In the *Process*, *Mesh*, *Cell Mesh* section select *Fix Corners*.
    11.2. Click *Go*.
    11.3. In the *Segmentation* section, choose *Watershed Segmentation*.

  11.4. Click *Go*.

  11.5. The corners should now be fixed.

12. If you are not satisfied with the smoothness of the boundaries:

  12.1. In the *Process*, *Mesh*, *Structure* section select Subdivide Adaptive Near Borders.

  12.2. Map the signal data onto the mesh again using the procedure described previously at step 19 in the section "Building the Mesh".

  12.3. In the *Process*, *Segmentation* section select *Watershed Segmentation*.

  12.4. Use the default parameters.

  12.5. Click *Go*.

13. Expand the *Cell Mesh* section and select *Convert to Cells*.

14. Choose a value of 1μm for the *Minimum Distance* parameter.

    - This determines the smallest wall segment.
    - Smaller values increase the number of points in the final dataset.
    - Larger values decrease the number of points but may miss small details in the cell boundaries.
    - The mesh should now look similar to 2.3C and 2.3D.

15. Save the cell data.

  15.1. From the top menus, select the *Mesh* dropdown menu.

  15.2. Select *Mesh 1*, then *Export*.

  15.3. Choose *Cells* for the file type.

      - This creates a text file will coordinates of cell boundaries only.
      - The entire mesh data is not included.

  15.4. Click *OK*.

16. Save the mesh.

  16.1. From the top menus, select the *Mesh* dropdown menu.

  16.2. Select *Mesh 1*, then *Save*.

  - This creates a .mgxm file.
  - All of the mesh data is included.
  - This file can be used to re-load the mesh later.

16.3. Click *OK*.

When errors are received while trying to create cells (step 13), there sometimes was a problem with the structure of the mesh. The following Python code was used to try to fix the problem. After running this code, the steps at 13 were used to build the cells again.

```
Mesh.Segment_Mesh(20000)
count = 0
while count < 2:
    try:
        Mesh.Make_Cells(1)
        break
    except:
        Mesh.Fix_Corners()
        Mesh.Smooth_Mesh(1)
        Mesh.Segment_Mesh(20000)
    count += 1
```

At this point the data is exported as a text file (as created in step 15). This file contains the coordinates of all the cell boundaries. This can then be used in the analysis of DR5 expression in the meristem as described in section 2.2.3.

2.3 Results

Though we know a lot about the mechanisms of polar auxin transport, we don't fully understand which parts of that system are the most sensitive. Or to put it another way, when perturbed, which parts cause the greatest change in phenotype? To understand this better, I first created computer models to easily tune different parameters. These models led to a number of hypotheses which I then tested.

Figure 2.4: Examples of the graphical output from L-systems. The cells grow over a semi-realistic SAM geometry. Outgrowth of primordia is purely visual and does not affect the functioning of the model in any way.

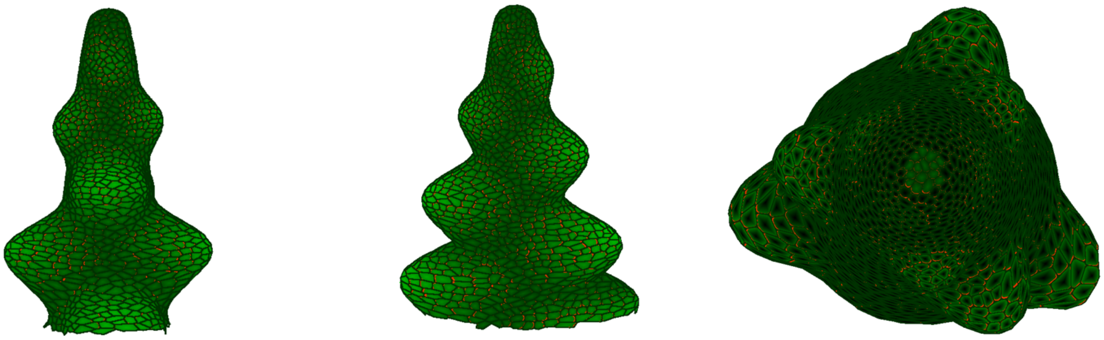

(a) Decussate phyllotaxis (b) Alternate phyllotaxis (c) Spiral phyllotaxis

2.3.1 Phyllotaxis Model

Previously, Richard Smith and colleagues created a model of phyllotaxis that incorporated polar auxin transport on a growing mesh of cells that simulate semi-realistic SAM geometry[105]. This model was built in the L-Systems software package in C++ and compiled to run on a Windows operating system. I borrowed this software package and modified the model to incorporate some of the biochemical equations put forth by Jönsson *et al*[107]. This model is capable of generating all of the phyllotaxis patterns commonly observed in plants. Figure 2.4 shows examples of the graphical output. The cells grow and divide over the geometry of a paraboloid. The primordia that grow out from the sides of the paraboloid are only visual and the geometry of the cellular mesh is not actually stretched.

Due to the particular math involved in this model, running it takes a considerable amount of time on a standard laptop. In order to try many different parameter combinations I developed a system for running this software on Amazon's EC2 cloud service. This allows for the model to run on an arbitrary number of computers simultaneously each with a different combination of parameters. My software sends parameters combinations to each model instance and reads the output of each instance, which is composed of a series of divergence angles and plastochron times in text form.

After trying many different values for individual model parameters I found that two of the parameters which effected the phyllotaxis pattern the most were the size of the meristem tissue and the size of the cells. To explore that space more, I tuned both of those parameters, trying each possible pair of values within a certain range, while leaving all other parameters untouched. The results of that experiment are plotted in Figure 2.5.

Figure 2.5

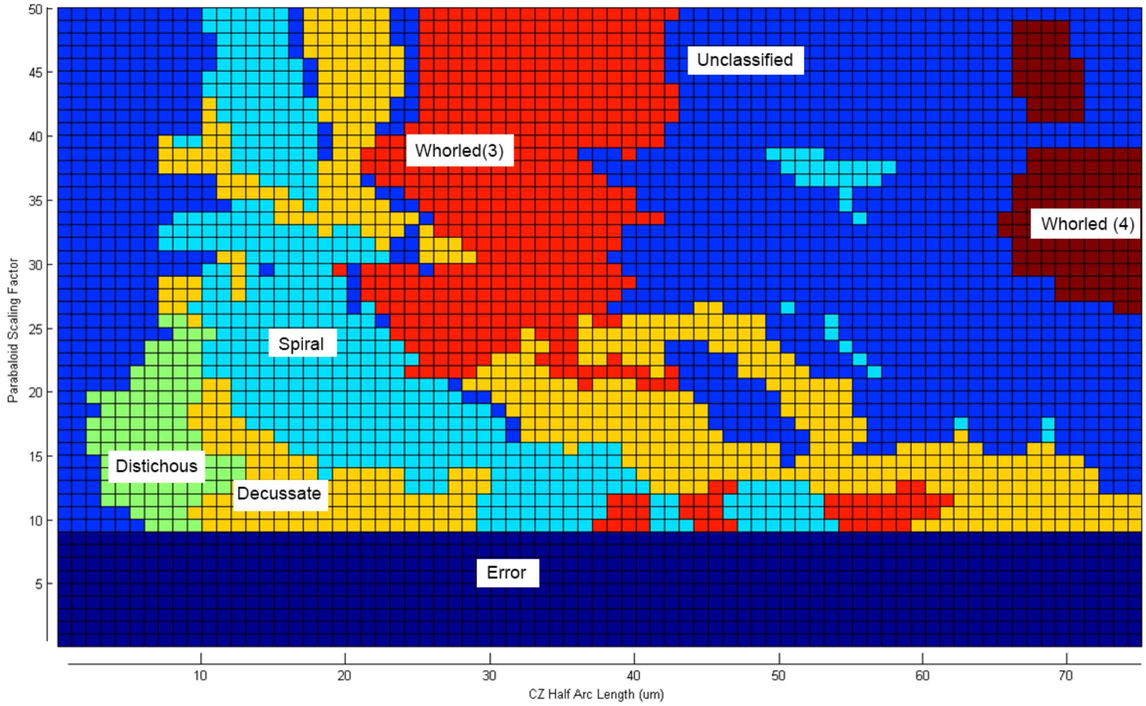

The phyllotaxis patterns were classified into discrete groups (spiral, alternate, etc) which are color coded. It is clear from this plot that the pattern remains steady within particular ranges and then abruptly switches to a different pattern rather than randomly quickly switching between different patterns. This suggests that the model is a multi-stable system with large contiguous parameter spaces that all converge on the same output.

2.3.2 Modeling Auxin Movement

In this complex model, cell size appears to play a major part in controlling the phyllotaxis pattern. This could be due to the fact that diffusion within individual cells is not considered (within this particular model). Once a molecule of auxin is transported into a cell it is free to diffuse out of or be transported across any other membrane. *In vivo* diffusion through individual cells definitely occurs but it may have little effect if the rate of other processes (transport across membranes) is slow compared to intracellular diffusion. This means auxin is always well mixed and there is no auxin gradient across a cell. To explore this phenomenon further I created a simple cellular model of auxin diffusion through a single file of rectangular cells implemented in SciPy with functions derived from Cellzilla[116] and Cellerator[117].

In this model passive diffusion across membranes is ignored. Only two factors are considered: transport across membranes between neighbouring cells and diffusion within cells. These factors are modelled using the Cellerator diffusion function $\{X \to X, \mathrm{Diffusion}[f[i,j,k]]\}$ and the Cellzilla transport function $\{X \to X, \mathrm{Transport}[\mathrm{fout}, \mathrm{fin}]\}$. These two functions represent the equations for Fick's law of diffusion

$$J = -D\frac{\partial X}{\partial x} \tag{2.1}$$

and this equation representing facilitated membrane transport

$$\frac{d[X_i]}{dt} = \frac{\ell_k}{A_i}(f_{in}(i,j,k)) - f_{out}(i,j,k) - f_{in}(i,j,k) + f_{out}(i,j,k)) \tag{2.2}$$

Each cell is broken up into many individual elements (finite element method) so that diffusion through the cell can be easily calculated. The transport function is only applied to the elements at the boundaries of the cells.

First, a model was created with 175 cells and was run both with diffusion (2.6A) and without diffusion (2.6B). The model was started with randomized initial auxin concentrations in each cell and ran until a steady state was reached where auxin was no longer transported. As the model runs auxin is transported to the neighbouring cell with the highest auxin concentration. This leads to regions of high and low concentrations of auxin, or "peaks" and "valleys." When the model is run to a steady state condition the peaks turn into single cells containing all of the auxin and valleys containing none. This condition may not actually be encountered *in vivo* but gives a simple method to quantify the number and spacing of peaks: count the cells with greater than zero auxin.

Initially, the parameters of diffusion were intentionally tweaked so that the number of peaks was nearly identical in both the diffusion and diffusion-free models. Then a second model was created with one third as many cells but each cell being three times as wide and having three times as many elements. This model was also run with diffusion (2.6C) and without diffusion (2.6D) using the same diffusion parameters as before.

Then the models were each run 100 times for each condition (400 times total) to determine the average number of "auxin peaks" under each condition. These results show that when intracellular diffusion is considered the spacing of auxin peaks is nearly identical. The auxin peaks accumulate at approximately the same distances apart but with fewer cells in between. When intracellular diffusion is ignored, the spacing of the auxin peaks is dependent on the size of the cells. Auxin peaks

Figure 2.6: Finite Element 1-Dimensional Model of Auxin Transport. **A.** Small cells *with* diffusion. **B.** Small cells *without* diffusion. **C.** Large cells *with* diffusion.**D.** Large cells *without* diffusion.

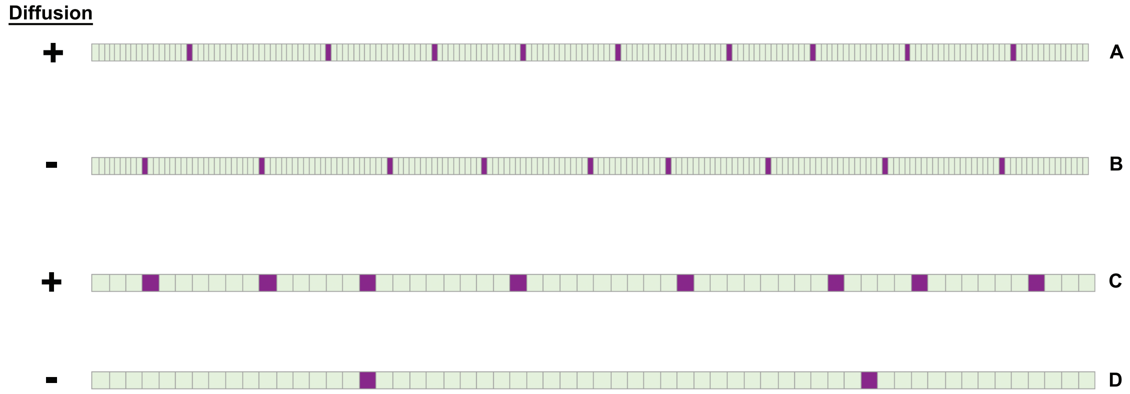

accumulate at different distances apart but with approximately the same number of cells between peaks.

If we assume that *in vivo* intracellular diffusion is rapid compared to intercellular transport then morphological features that result from auxin accumulation should be altered in plants with different sized cells.

2.3.3 Shoot Apical Meristem

Auxin accumulates in small regions around the periphery of the meristem at the sites of future organ primordia. The auxin reporter, DR5, is transcribed in high levels in about five to ten cells in each of these regions. Typically these regions form approximately 137 from the last region. Although this tissue is a more complex system than a simple line of rectangular cells, if cell size does play a significant part in controlling the distribution of auxin, the effect should be measurable in mutants with abnormal cell size.

To study the effects that cell size has on auxin distribution in the shoot meristem, auxin transcriptional reporters were added to mutant lines with abnormal cell sizes. The reporter used was pDR5::2xGFP-N7, a nuclear localized GFP that is expressed in areas of high auxin concentration. This reported was transformed into five lines: Ler, Col-0, Wa-1, cycd3;1-3, and msc3. See table 2.1. Transformants were self-crossed to generate homozygous reporter lines. Chosen homozygous reporter lines were picked based on high GFP expression in the roots which is visible under an epifluorescent dissecting microscope.

Table 2.1: Lines Transformed with DR5 Reporter

Name	**Cells**	**Selection**	**Note**
Ler	Wt	Kanamycin	
Col-0	Wt	Kanamycin	
Wa-1	Large	Kanamycin	Tetraploid ecotype
cycd3;1-3	Large	Hygromycin	Triple Cyclin mutant, mixed background
msc3	Small	Kanamycin	Allele of SQN (cyclophilin 40) gene

Figure 2.7: Comparison of cell sizes in the shoot apical meristem. Two wild type ecotypes and three mutants.

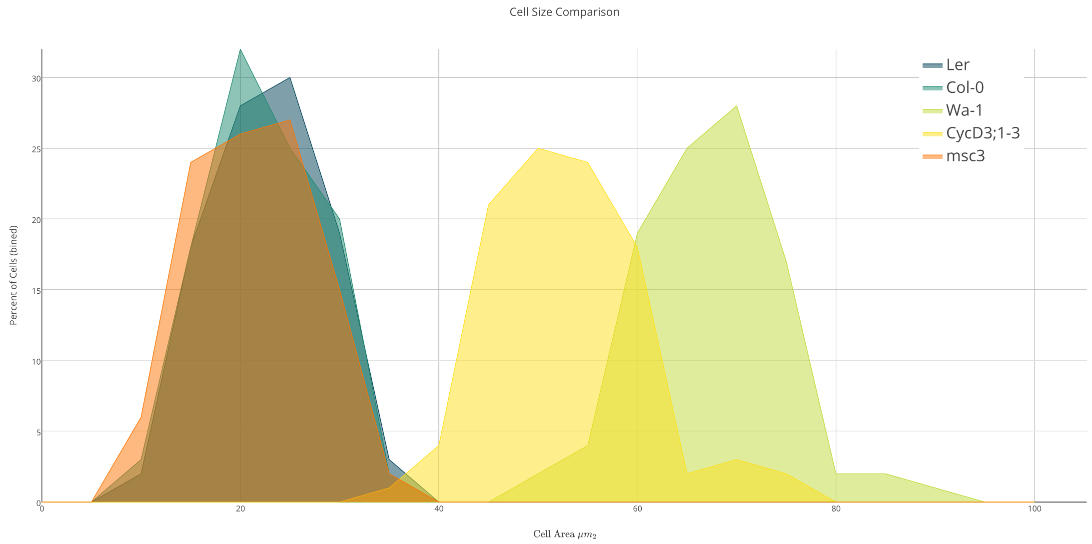

These three mutants were previously reported to have abnormal cell sizes. Wa-1, a tetraploid ecotype, is taller than wild type with a thicker stem, leaves with a larger surface area, and is reported to have larger cells throughout the plant. *cycd3;1-3*, a triple Cyclin mutant, also is taller, thicker, and has broader leaves than wild type, and is reported to have larger cells. *msc3*, an allele of the SQN gene in the Col-0 background, is approximately the same size as Col-0 and has smaller but more numerous cells throughout the plant. To quantify the extent of the cell size abnormalities in the meristem, five meristems from each line were stained with FM4-64 (a fluorescent, lipophilic membrane dye), imaged with laser scanning confocal microscopy, and then processed with MorphoGraphX (see section 2.2.11) to extract the geometry of the cells in the first epidermal layer.

The geometric data extracted from MorphoGraphX were used to calculate the 2-dimensional areas of each cell in each meristem using a custom Python script. The results of this analysis are shown in Figure 2.7. Both wild type lines have approximately the same distribution of cell sizes in the meristem around $20\mu m^2$. The large cell mutants both have cell areas larger than wild type with

Figure 2.8: DR5 expression in the shoot apical meristem. Processed in MorphoGraphX to only show a projection from the first layer of cells. *Red:* FM4-64. *Green:* pDR5::2xGFP-N7. Scale bar is 20μm

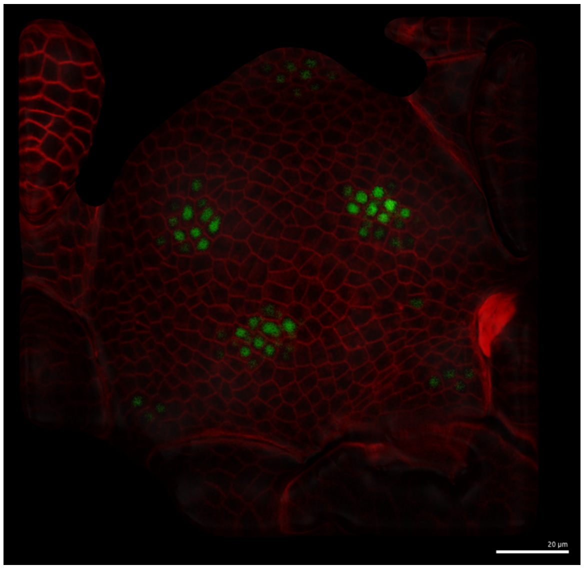

cycd3;1-3 around $50\mu m^2$ and Wa-1 cells around $70\mu m^2$. *msc3* cells on the other hand were around the same size as wild type cells, around $20\mu m^2$. Further analysis of this line showed that cells in the leaves, roots, and shoot were in fact smaller than wild type as reported.

One possible explanation for this lack of small cells in the SAM is that these cells are already at a minimum size. This lower limit could be set by the size of the nucleus, which could be determined by the size of the chromosomes it contains. In an attempt to lower the minimal cells size in the meristem, the *msc3* line was crossed to *cenh3-1/+ GFP-tailswap/GFP-tailswap*, a line able to induce haploidy[118]. Seeds from this cross either did not germinate or were not haploid, suggesting this particular combination of mutants is embryonic lethal.

To quantify the distribution pattern of auxin in these cell size mutants, the plants were imaged as before this time capturing FM4-64 on one channel and GFP on a second channel as shown in Figure 2.8. The 2-channel images were processed with MorphoGraphX to extract the geometry of the first layer of cells and also classify segmented cells as either DR5 positive or negative, as shown in figure 2.9. This was done for all of the mutants, as shown in figure 2.10.

Using the data extracted with MorphoGraphX, the distances and number of cells between each of the DR5 regions were calculated using a custom Python script. Cells labeled as DR5-positive cells were grouped manually. A centroid (arithmetic mean of points) was calculated using the center of each DR5-positive as an equally weighted point. These centroids were used as the reference points

Figure 2.9: Meristems segmented using MorphGraphX to extract the geometry of the first layer of epidermal cells. *Left:* The segmented cell geometry. *Center:* Cell geometry overlayed with the DR5 signal extracted from the first layer. *Right:* Segmented cells containing DR5 labelled to differentiate them from non-DR5 expressing cells.

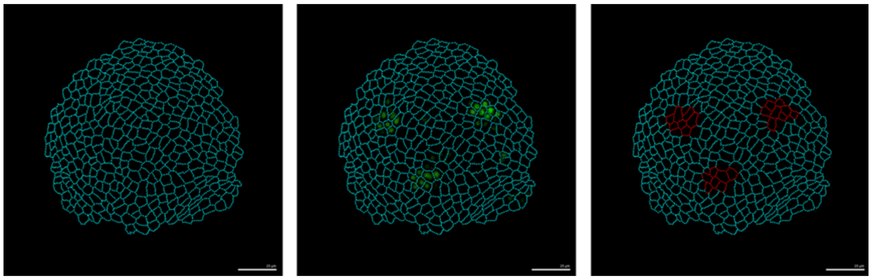

Figure 2.10: Three DR5 Meristem Comparison

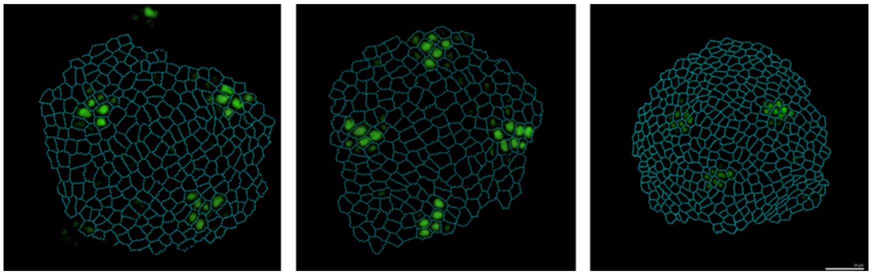

when calculating distances and number of cells. The results of these measurements are shown in figure 2.11.

The difference between wild type and *msc3* and large cell mutants is clear when looking at absolute distances between DR5 regions. The DR5 regions are almost twice as far apart in the large cell mutants compared to wild type and *msc3*. But the difference is not so clear when looking at number of cells in between regions as the error in the measurements is relatively large. This could be due to the method in which the measurement was made. To make that measurement, any cell crossed by the shortest line between regions is counted, even if the line crossed only a small corner of the cell. Also, some regions of the meristem are dividing faster than other, as shown in the first chapter. If the line happens to cross through a region undergoing rapid division then more cells would be counted. Or it is possible that there really is a lot of variability between plants of the same line, or even the same meristem at different points in time. Capturing such variability using snapshots of a highly dynamic process is error prone and increasing the sample size may not yield any more interesting results without a fundamental change to the experiment. One such experiment could be live imaging many plants and quantifying how the number of cells between DR5 regions changes every couple of hours.

Figure 2.11: Distances between regions of DR5 expression in the SAM. **A:** Mean number of cells between regions of DR5 expression. **B:** Mean distance between regions of DR5 expression.

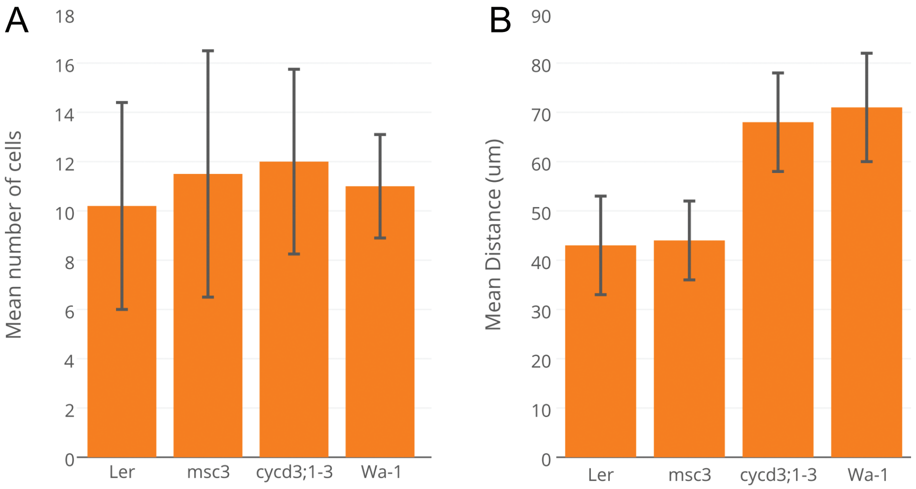

2.3.4 Shoots

During early shoot development it is thought that auxin is transported around the base of the vascular ring. In areas where auxin accumulates a vascular bundle is formed. If this is true then vascular development might be under the control of the same mechanisms at play in the meristem and the cell size dependent phenomenon shown in the model might be relevant.

To test this I looked at cross sections of shoots in wild type and cell size mutants to see if there was a correlation between number of cells and number of bundles. Tissue samples of mature plants were taken, fixed in formaldehyde, embedded in paraffin, sectioned, stained with Toluidine Blue O (to increase the contrast of the cells in the vasculature), mounted, and imaged. In the images I manually counted the number of bundles in each sample as seen in figure 2.12A. Additionally I used image processing techniques to assist in the counting of the cells at the base of the vascular ring, as seen in figure 2.12B.

The results of this study shown in figure 2.13 indicate that there is a linear relationship between the number of cells in the vascular ring and the number of bundles in adult shoot tissue. In general, more cells lead to more vascular bundles. Although, it is interesting to note that Wa-1 and *cycd3;1-3*

Figure 2.12: Paraffin embedded sections of the shoot showing vascular bundles stained with Toluidine Blue O. *A:* msc3 shoot showing 9 vascular bundles. *B:* Cells at the base of the vascular ring are counted.

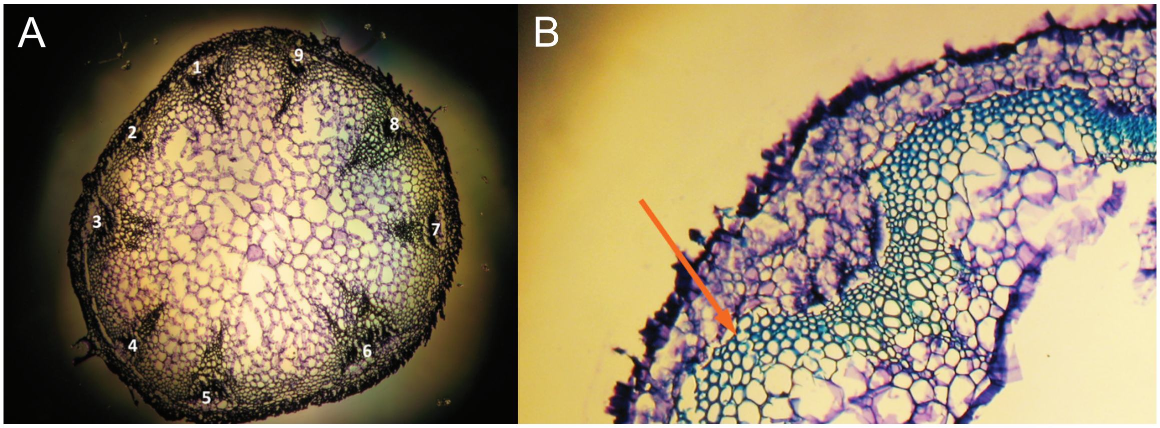

did not have the fewest number of cells, which is what would be assumed if the cells were larger and the shoot was the same size compared to wild type. In these mutants which have more cells than wild type, the vascular cells are in fact larger but the shoot is also larger, which more than makes up for the larger cells. Despite this observation, the more cells more bundles relationship holds up.

2.3.5 Roots

In the roots of Arabidopsis, lateral roots develop in an alternating pattern out of the sides of the primary root, usually on the outside edge of a curve. To test if the transport-limited model is at play in this case, large and small cell mutants with the pDR5::2xGFP-N7 reporter were observed. The plants were grown on MS agar and individual plants were removed and imaged at one, three and ten days after germination. These plants were stained with FM4-64 to label the cell membranes and then observed with laser scanning confocal microscopy.

Initially the goal was to find the areas of DR5 expression along the root and using image processing techniques measure the distance and number of cells between these areas. But the images showed that the expression of DR5 in the roots of cell size mutants, particularly the large cell mutants *cycd3;1-3* and Wa-1, was disorganized compared to wild type. In Wa-1 at one day after germination, as shown in Figure 2.14A, there is a repeating DR5 pattern similar to wildtype (pairs of DR5 expressing cells periodically up the root with increasing space in between higher on the root) but with rapidly decreasing intensity as the expressing cells are pushed further from the meristem.

Figure 2.13: Relationship between number of vascular bundles in the shoot and the number of cells around the base of the vascular ring.

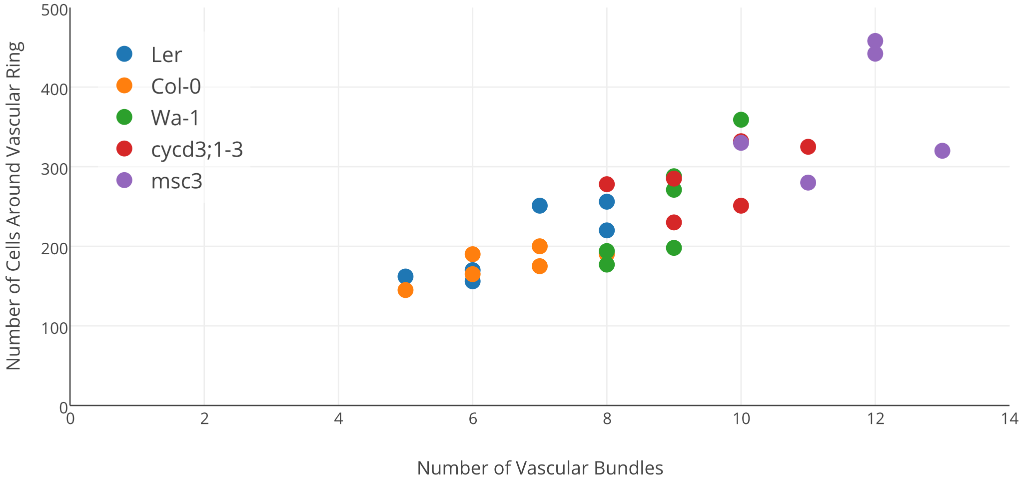

Three days after germination (Figure 2.14B) the pairs of DR5 expressing cells above the meristem have turned into a mass of seeming randomly arranged DR5 expressing cells with a single file of DR5 expressing cells progressing basally away from the meristem. By ten days after germination (Figure 2.14C) the root has enlarged, the meristem has become completely disorganized with DR5 expressing cells scattered throughout, and no DR5 expression basal to the meristem. But despite this breakdown in auxin signalling, or at least in the expression of one particular auxin-sensitive promoter, the plant still makes wild type looking lateral roots at the sites of curvature.

Given that auxin is a critical component in our model, it is difficult to imagine how the transport limited model could be accurate in the root given the disorganization displayed by the auxin reporter.

2.3.6 Leaves

During leaf formation, auxin is transported around the periphery of the leaf primordium. Leaf serrations or teeth develop in the areas of high auxin accumulation. Although this is a highly dynamic system like the SAM, one could image the ring of cells along the perimeter being stretched out into a straight line like the simple linear model described earlier. If the assertion that the cells are well mixed (or at least sufficiently mixed given the rate of intercellular transport) is true then

Figure 2.14: Progression of the DR5 expression pattern in Wa-1 root tips. *A:* One day after germination. *B:* Three days after germination. *C:* Ten days after germination.

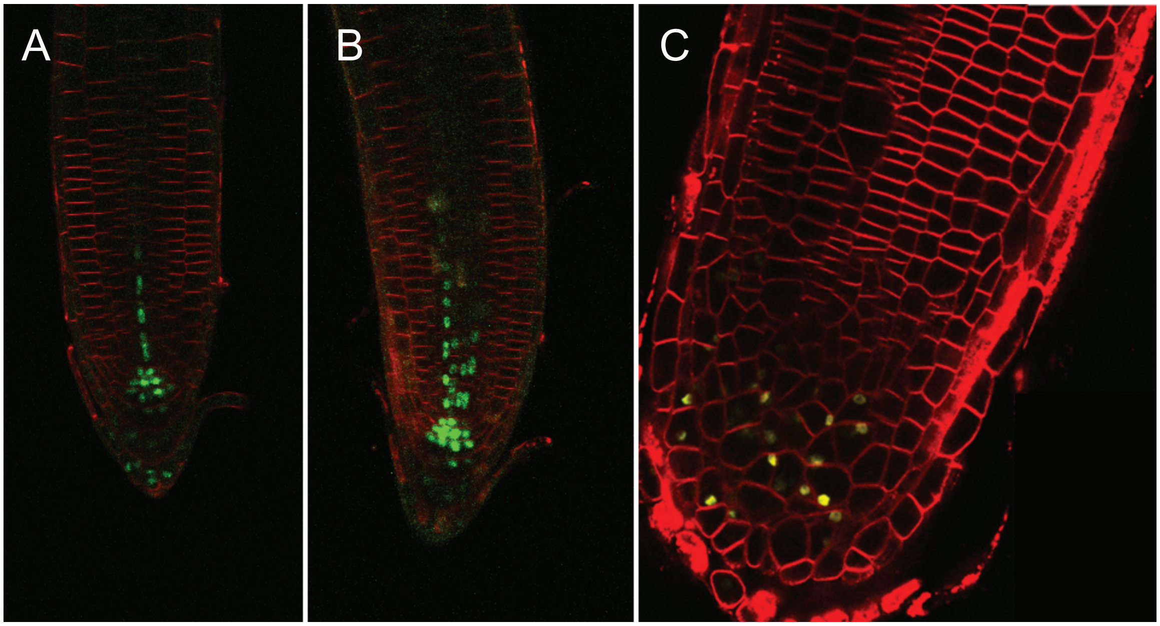

we should expect the spacing of the leaf serrations to be dependent on cell size. Plants with larger cells but the same size leaf as wild type should have fewer teeth. The cell size mutants considered here do in fact have similar size leafs to wild type even though their cells are different sizes.

To quantify this phenomenon 100 leaves were collected from each line, two per plant. The leaves were flattened and the side of the leaf with the most well defined teeth was chosen and the teeth were counted on that side, as shown in figure 2.15. The results from these observations (Figure 2.16) show that the large cell mutants have fewer teeth than wild type while the small cell mutant has more teeth than wild type on average, though, the magnitude of the effect is not as large as one might expect. The cells in Wa-1 and *cycd3;1-3* are at least twice as large as wild type but only have about 25% fewer teeth. Likewise, *msc3* mutants only have about 25% more teeth than wild type.

Given that the cells in Wa-1 and *cycd3;1-3* have approximately twice the diameter and four times the area of wild type cells, one might expect Wa-1 and *cycd3;1-3* leaves to have half as many serrations. So the linear model auxin-gradient-free model does not fully explain this phenomenon.

Figure 2.15: Rosette leaves from wild type and cell size mutant plants. Serrations are counted along one side of a leaf. *A:* Col-0. *B:* CycD3;1-3. *C:* Wa-1. *D:* msc3.

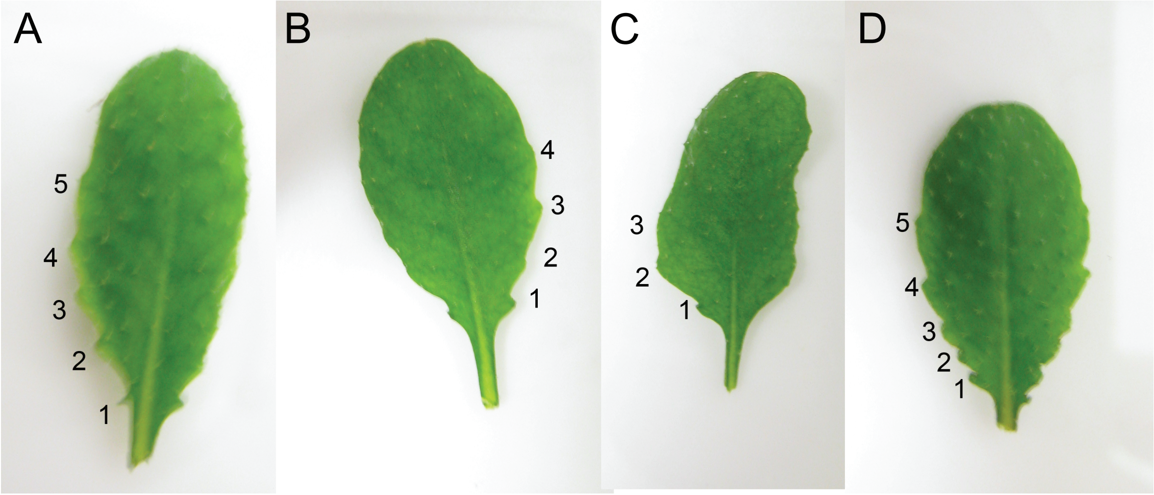

Figure 2.16: Mean number of teeth per rosette leaf. Sample size was 100 leaves per line. Teeth counted on one side of leaf.

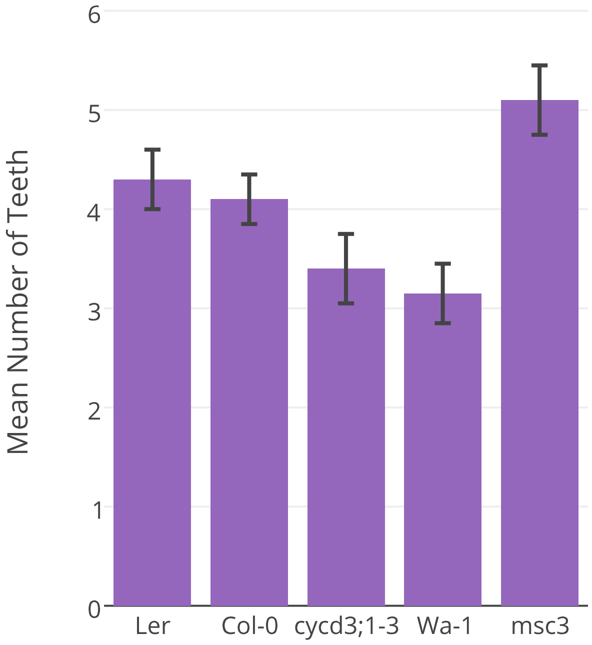

2.4 Discussion

Previous work in this field has determined that auxin accumulation is often responsible for organ formation and tissue differentiation. In areas of the plant where auxin accumulates cells expand and divide rapid and differentiate. It has been shown that polar auxin transporters play a key role in the distribution of auxin and therefore control morphogenesis. Currently there are two competing explanations for how these polar auxin transports chose the direction to pump auxin. One is that (through an unknown mechanism) the PIN protein are localized to the membrane adjacent to the neighboring cell with the highest auxin concentration and pump auxin towards that cell. The other is that PIN proteins localize to the side of the cell which is transporting the most auxin and transport more auxin, leading to a positive feedback loop. But given all that is known about this system, none of this explains how the spacing between auxin maxima is determined or controlled.

Here I have shown that cell size is a critical factor in controlling the accumulation of auxin in certain parts of the plant. The model predicts that when transport across the membrane is the rate limiting step, auxin accumulates in regions separated by a consistent number of cells rather than a consistent distance. I tested this by looking at auxin and organ spacing in mutants with different cell diameters. If the model is to be believed then organs should have larger spaces between them in plants with larger cells and smaller spaces in plants with smaller cells.

In the shoot apical meristem, at least during its reproductive phase, the spacing of the floral primordia is affected by the size of the cells. The absolute distance between primordia as measured along the surface of the meristem is about 75% greater in large cell mutants compared to both wild type and *msc3*, which has the same sized cells as wild type in the SAM. When looking at the number of cells between primordia, the average number of cells is approximately the same in all mutants, which supports the model's predictions. But the variability in those particular measurements is great enough that it is possible that there really is a difference in cell numbers between large cell mutants and wild type and the difference is just hidden in the noise.

The amount of variability may be an artifact of the particular measurement used. To measure the number of cells between primordia, a line was created in software between the centers of the primordia being measured. This line followed the curvature of the meristem surface and intersected with cell boundaries. The number of intersections n were counted to determine the number of cells in between the primordia, $n + 1$. Sometimes the line would pass through a very small section of the corner of a cell, which would not contribute much to the distance but would increase the cell count by one. Considering the small number of cells between sequential primordia, adding an extra cell or two could increase the cell count by a relatively large amount. A different algorithm for measuring cell numbers might lead to results with smaller error bars.

In the shoot tissue, the spacing of the vascular bundles also seems to be affected by cell size. It is thought that during early development auxin is transported around a ring of cells in the shoot. In areas where auxin accumulates the tissue differentiates and forms vascular bundles. I have shown that in large and small cell mutants the number of vascular bundles is tightly correlated with the number of cells in the vascular ring. However, in this study the shoot tissue was observed long after the vascular bundles had formed and the size of the cells in the mature tissue probably had no influence on vascular structure. It is possible that during the developmental stage where auxin distribution affected vascular bundle formation the cells in the mutants were also of larger or smaller size, which would support the model.

Previous work has shown that in early leaf primorida, auxin accumulates in areas around the periphery of the leaf [119]. In these areas of high auxin concentration, serrations are formed. If we assume that auxin transport is behaving similar to the model and that the leaves in cell size mutants have the same circumference as wild type then we would expect the number of serrations to vary in proportion to the cell size. The size of leaves in cell size mutants turns out to not be exactly the same as wild type but is similar enough to make a comparison. I observed large cell mutants to have fewer serrations than wild type and the small cell mutant to have more serrations than wild type. The proportions are not exactly what is expected given the magnitude in change of cell size but this could be due to differences in leaf primordia size between the mutants. For example, in large cell mutants a fewer-serrations phenotype due to larger cells could be masked by a larger primordia, which would increase the number of cells and therefore the number of serrations. Nevertheless the direction of change is in agreement with the model suggesting that auxin movement in the leaf is transport limited rather than diffusion limited.

In roots, auxin is thought to play a role in meristem maintenance and also in the formation of lateral roots. If the positioning of the lateral roots is determined by transport-limited auxin movement rather than diffusion-limited movement (or some other mechanism) then large and small cell mutants should show differences in spacing between lateral roots. In this study I observed that auxin distribution, or at least the expression of DR5 (which should be an accurate proxy for auxin distribution), basal of the meristem is disorganized in large and small cell mutants. Yet those plants make a typical number of lateral roots that appear to be phenotypically normal.

One possible explanation for this observation is that auxin distribution is normal in these mutants while DR5 expression is altered and is not acting as a proxy for auxin concentration due to some interference in the upstream auxin signalling pathway. I find this explanation to be unlikely as DR5 expression is normal throughout other parts of the plant in cell size mutants. It is possible that the roots have a slightly different auxin signalling pathway than the above-ground tissue that is particularly sensitive to some difference in the cell size mutants. Additionally, if auxin signalling was actually interrupted in the roots, one would expect other parts of the roots to have phenotypic abnormalities which were not observed.

Another possible explanation is that auxin is not necessary for the patterning of lateral roots. It has been shown that auxin accumulates at bends in the root where a lateral root primordia eventually forms. It has also been shown that auxin is critical to the formation of lateral roots as this tissue is malformed in auxin synthesis mutants. Taking these observations as fact, it is still possible for auxin to not be necessary for the positioning of the lateral roots. For example, the accumulation of auxin at the future sites of lateral roots primordia may be coincidental rather than directly upstream of primordia formation like in the shoot meristem. One could imagine a mechanism (X) that causes both auxin accumulation (Y) and lateral root formation in the same location (Z). In this hypothetical scenario X could cause Y and Z ($X \rightarrow Y, X \rightarrow Z$) but Y may not be responsible for causing Z ($X \rightarrow Y \rightarrow Z$). In this scenario the cell size mutants could interfere with auxin distribution without the need for an alternative signalling pathway and still have normal lateral root formation in both the positioning of the primordia and the development of primordia into mature roots.

Overall, the auxin transport limited model is substantiated by observations in the shoot apical meristem, shoot vasculature, and to some extent in the leaves. It is not supported by observations of the root. It is possible that auxin distribution is controlled by two different mechanisms above and below ground, or that a single mechanism (different than the one described) is responsible for all tissue and the observations supporting the model were coincidental. Nevertheless, further experiments will be needed to fully understand the relationship between cell size and auxin distribution.

References

[1] Charles Darwin and Francis Darwin. *The Power of Movement in Plants.* London: John Murray Publishers, 1880.

[2] Fritz Kogl and Arie Jan Haagen-Smit. "Mitteilung uber pflanzliche wachstumsstoffe. Uber die vhemie des euchsstoffs". In: *Proc. K. Ned. Akad. Wet* 34 (1931), pp. 1411–1416.

[3] I. Casimiro. "Auxin Transport Promotes Arabidopsis Lateral Root Initiation". In: *The Plant Cell* 13.4 (Apr. 2001), pp. 843–852. ISSN: 10404651.

[4] I Barlier et al. "The SUR2 gene of Arabidopsis thaliana encodes the cytochrome P450 CYP83B1, a modulator of auxin homeostasis." In: *Proceedings of the National Academy of Sciences of the United States of America* 97.26 (Dec. 2000), pp. 14819–24. ISSN: 0027-8424.

[5] J Normanly, J D Cohen, and G R Fink. "Arabidopsis thaliana auxotrophs reveal a tryptophan-independent biosynthetic pathway for indole-3-acetic acid." In: *Proceedings of the National Academy of Sciences of the United States of America* 90.21 (Nov. 1993), pp. 10355–9. ISSN: 0027-8424.

[6] J Ouyang, X Shao, and J Li. "Indole-3-glycerol phosphate, a branchpoint of indole-3-acetic acid biosynthesis from the tryptophan biosynthetic pathway in Arabidopsis thaliana." In: *The Plant Journal* 24.3 (Nov. 2000), pp. 327–33. ISSN: 0960-7412.

[7] Andrew W Woodward and Bonnie Bartel. "Auxin: regulation, action, and interaction." In: *Annals of Botany* 95.5 (Apr. 2005), pp. 707–35. ISSN: 0305-7364.

[8] Yunde Zhao et al. "Trp-dependent auxin biosynthesis in Arabidopsis: involvement of cytochrome P450s CYP79B2 and CYP79B3." In: *Genes & Development* 16.23 (Dec. 2002), pp. 3100–12. ISSN: 0890-9369.

[9] S Bak et al. "CYP83B1, a cytochrome P450 at the metabolic branch point in auxin and indole glucosinolate biosynthesis in Arabidopsis." In: *The Plant Cell* 13.1 (Jan. 2001), pp. 101–11. ISSN: 1040-4651.

[10] Michael Dalgaard Mikkelsen, Peter Naur, and Barbara Ann Halkier. "Arabidopsis mutants in the C-S lyase of glucosinolate biosynthesis establish a critical role for indole-3-acetaldoxime in auxin homeostasis". In: *The Plant Journal* 37.5 (Mar. 2004), pp. 770–777. ISSN: 0960-7412.

[11] J Normanly et al. "Arabidopsis mutants resistant to the auxin effects of indole-3-acetonitrile are defective in the nitrilase encoded by the NIT1 gene." In: *The Plant Cell* 9.10 (Oct. 1997), pp. 1781–90. ISSN: 1040-4651.

[12] Satoko Sugawara et al. "Biochemical analyses of indole-3-acetaldoxime-dependent auxin biosynthesis in Arabidopsis." In: *Proceedings of the National Academy of Sciences of the United States of America* 106.13 (Mar. 2009), pp. 5430–5. ISSN: 1091-6490.

[13] Anna N Stepanova et al. "TAA1 mediated auxin biosynthesis is essential for hormone crosstalk and plant development." In: *Cell* 133.1 (May 2008), pp. 177–91. ISSN: 1097-4172.

[14] Yi Tao et al. "Rapid synthesis of auxin via a new tryptophan-dependent pathway is required for shade avoidance in plants." In: *Cell* 133.1 (Apr. 2008), pp. 164–76. ISSN: 1097-4172.

[15] Kiyoshi Mashiguchi et al. "The main auxin biosynthesis pathway in Arabidopsis." In: *Proceedings of the National Academy of Sciences* 108.45 (Nov. 2011), pp. 18512–7. ISSN: 1091-6490.

[16] Christina Won et al. "Conversion of tryptophan to indole-3-acetic acid by TRYPTOPHAN AMINOTRANSFERASES OF ARABIDOPSIS and YUCCAs in Arabidopsis." In: *Proceedings of the National Academy of Sciences of the United States of America* 108.45 (Dec. 2011), pp. 18518–23. ISSN: 1091-6490.

[17] Y Zhao et al. "A role for flavin monooxygenase-like enzymes in auxin biosynthesis." In: *Science* 291.5502 (Jan. 2001), pp. 306–9. ISSN: 0036-8075.

[18] Youfa Cheng, Xinhua Dai, and Yunde Zhao. "Auxin synthesized by the YUCCA flavin monooxygenases is essential for embryogenesis and leaf formation in Arabidopsis." In: *The Plant Cell* 19.8 (Aug. 2007), pp. 2430–9. ISSN: 1040-4651.

[19] Xinhua Dai et al. "The biochemical mechanism of auxin biosynthesis by an arabidopsis YUCCA flavin-containing monooxygenase." In: *The Journal of biological chemistry* 288.3 (Jan. 2013), pp. 1448–57. ISSN: 1083-351X.

[20] Patricia Hornitschek et al. "Phytochrome interacting factors 4 and 5 control seedling growth in changing light conditions by directly controlling auxin signaling." In: *The Plant Journal* 71.5 (Sept. 2012), pp. 699–711. ISSN: 1365-313X.

[21] Lin Li et al. "Linking photoreceptor excitation to changes in plant architecture." In: *Genes & Development* 26.8 (Apr. 2012), pp. 785–90. ISSN: 1549-5477.

[22] Jiaqiang Sun et al. "PIF4-mediated activation of YUCCA8 expression integrates temperature into the auxin pathway in regulating arabidopsis hypocotyl growth." In: *PLoS genetics* 8.3 (Jan. 2012). Ed. by Li-Jia Qu, e1002594. ISSN: 1553-7404.

[23] D Magnus Eklund et al. "The Arabidopsis thaliana STYLISH1 protein acts as a transcriptional activator regulating auxin biosynthesis." In: *The Plant Cell* 22.2 (Feb. 2010), pp. 349–63. ISSN: 1532-298X.

[24] L Galweiler et al. "Regulation of polar auxin transport by AtPIN1 in Arabidopsis vascular tissue." In: *Science* 282.5397 (1998), p. 30. ISSN: 0036-8075.

[25] Misuk Cho, Sang Ho Lee, and Hyung-Taeg Cho. "P-glycoprotein4 displays auxin efflux transporter-like action in Arabidopsis root hair cells and tobacco cells." In: *The Plant Cell* 19.12 (Dec. 2007), pp. 3930–43. ISSN: 1040-4651.

[26] Markus Geisler et al. "Cellular efflux of auxin catalyzed by the Arabidopsis MDR/PGP transporter AtPGP1." In: *The Plant Journal* 44.2 (Oct. 2005), pp. 179–94. ISSN: 0960-7412.

[27] Kamil Ruzicka et al. "Arabidopsis PIS1 encodes the ABCG37 transporter of auxinic compounds including the auxin precursor indole-3-butyric acid." In: *Proceedings of the National Academy of Sciences of the United States of America* 107.23 (June 2010), pp. 10749–53. ISSN: 1091-6490.

[28] M J Bennett et al. "Arabidopsis AUX1 gene: a permease-like regulator of root gravitropism." In: *Science* 273.5277 (Aug. 1996), pp. 948–50. ISSN: 0036-8075.

[29] R Swarup et al. "Localization of the auxin permease AUX1 suggests two functionally distinct hormone transport pathways operate in the Arabidopsis root apex." In: *Genes & Development* 15.20 (Oct. 2001), pp. 2648–53. ISSN: 0890-9369.

[30] Jan Petrásek et al. "PIN proteins perform a rate-limiting function in cellular auxin efflux." In: *Science* 312.5775 (May 2006), pp. 914–8. ISSN: 1095-9203.

[31] Justyna Wisniewska et al. "Polar PIN Localization Directs Auxin Flow in Plants". In: *Science* 312.May (2006), p. 2006.

[32] Pankaj Dhonukshe et al. "Auxin transport inhibitors impair vesicle motility and actin cytoskeleton dynamics in diverse eukaryotes." In: *Proceedings of the National Academy of Sciences of the United States of America* 105.11 (Mar. 2008), pp. 4489–94. ISSN: 1091-6490.

[33] Jürgen Kleine-Vehn et al. "Recycling, clustering, and endocytosis jointly maintain PIN auxin carrier polarity at the plasma membrane." In: *Molecular Systems Biology* 7 (Jan. 2011), p. 540. ISSN: 1744-4292.

[34] Jozef Mravec et al. "Cell plate restricted association of DRP1A and PIN proteins is required for cell polarity establishment in Arabidopsis." In: *Current Biology* 21.12 (June 2011), pp. 1055–60. ISSN: 1879-0445.

[35] Jing Zhang et al. "Inositol trisphosphate-induced Ca2+ signaling modulates auxin transport and PIN polarity." In: *Developmental Cell* 20.6 (June 2011), pp. 855–66. ISSN: 1878-1551.

[36] Pankaj Dhonukshe et al. "Generation of cell polarity in plants links endocytosis, auxin distribution and cell fate decisions." In: *Nature* 456.7224 (Dec. 2008), pp. 962–6. ISSN: 1476-4687.

[37] Niko Geldner et al. “The Arabidopsis GNOM ARF-GEF mediates endosomal recycling, auxin transport, and auxin-dependent plant growth.” In: *Cell* 112.2 (2003), p. 30. ISSN: 0092-8674.

[38] Jürgen Kleine-Vehn et al. “PIN auxin efflux carrier polarity is regulated by PINOID kinase-mediated recruitment into GNOM-independent trafficking in Arabidopsis.” In: *The Plant Cell* 21.12 (Dec. 2009), pp. 3839–49. ISSN: 1532-298X.

[39] Marta Michniewicz et al. “Antagonistic regulation of PIN phosphorylation by PP2A and PINOID directs auxin flux.” In: *Cell* 130.6 (Sept. 2007), pp. 1044–56. ISSN: 0092-8674.

[40] Lindy Abas et al. “Intracellular trafficking and proteolysis of the Arabidopsis auxin-efflux facilitator PIN2 are involved in root gravitropism.” In: *Nature Cell Biology* 8.3 (Mar. 2006), pp. 249–56. ISSN: 1465-7392.

[41] Yvon Jaillais et al. “AtSNX1 defines an endosome for auxin-carrier trafficking in Arabidopsis.” In: *Nature* 443.7107 (Sept. 2006), pp. 106–9. ISSN: 1476-4687.

[42] Yvon Jaillais et al. “The retromer protein VPS29 links cell polarity and organ initiation in plants.” In: *Cell* 130.6 (Sept. 2007), pp. 1057–70. ISSN: 0092-8674.

[43] Tomasz Paciorek et al. “Auxin inhibits endocytosis and promotes its own efflux from cells.” In: *Nature* 435.7046 (June 2005), pp. 1251–6. ISSN: 1476-4687.

[44] Stéphanie Robert et al. “ABP1 Mediates Auxin Inhibition of Clathrin-Dependent Endocytosis in Arabidopsis”. In: *Cell* 143.1 (Oct. 2010), pp. 111–121. ISSN: 00928674.

[45] Youfa Cheng et al. “NPY1, a BTB-NPH3-like protein, plays a critical role in auxin-regulated organogenesis in Arabidopsis.” In: *Proceedings of the National Academy of Sciences of the United States of America* 104.47 (Nov. 2007), pp. 18825–9. ISSN: 1091-6490.

[46] Masahiko Furutani et al. “The gene MACCHI-BOU 4/ENHANCER OF PINOID encodes a NPH3-like protein and reveals similarities between organogenesis and phototropism at the molecular level.” In: *Development* 134.21 (Nov. 2007), pp. 3849–59. ISSN: 0950-1991.

[47] Masahiko Furutani et al. “Polar-localized NPH3-like proteins regulate polarity and endocytosis of PIN-FORMED auxin efflux carriers.” In: *Development* 138.10 (May 2011), pp. 2069–78. ISSN: 1477-9129.

[48] Yuanting Li et al. “NPY genes play an essential role in root gravitropic responses in Arabidopsis.” In: *Molecular Plant* 4.1 (Jan. 2011), pp. 171–9. ISSN: 1752-9867.

[49] Johannes Leitner et al. "Lysine63-linked ubiquitylation of PIN2 auxin carrier protein governs hormonally controlled adaptation of Arabidopsis root growth." In: *Proceedings of the National Academy of Sciences of the United States of America* 109.21 (May 2012), pp. 8322–7. ISSN: 1091-6490.

[50] Marie Barberon et al. "Monoubiquitin-dependent endocytosis of the iron-regulated transporter 1 (IRT1) transporter controls iron uptake in plants." In: *Proceedings of the National Academy of Sciences of the United States of America* 108.32 (Aug. 2011), E450–8. ISSN: 1091-6490.

[51] P Green. "Phyllotactic Patterns: A Biophysical Mechanism for their Origin". In: *Annals of Botany* 77.5 (May 1996), pp. 515–528. ISSN: 03057364.

[52] D'Arcy Wentworth Thompson. *On Growth and Form*. Cambridge, UK: Cambridge University Press, 1942.

[53] Olivier Hamant et al. "Developmental patterning by mechanical signals in Arabidopsis." In: *Science* 322.5908 (Dec. 2008), pp. 1650–5. ISSN: 1095-9203.

[54] Naomi Nakayama et al. "Mechanical regulation of auxin-mediated growth." In: *Current biology : CB* 22.16 (Aug. 2012), pp. 1468–76. ISSN: 1879-0445.

[55] Heidi Szemenyei, Mike Hannon, and Jeff A Long. "TOPLESS mediates auxin-dependent transcriptional repression during Arabidopsis embryogenesis." In: *Science* 319.5868 (Mar. 2008), pp. 1384–6. ISSN: 1095-9203.

[56] T Ulmasov et al. "Aux/IAA proteins repress expression of reporter genes containing natural and highly active synthetic auxin response elements." In: *The Plant cell* 9.11 (Nov. 1997), pp. 1963–71. ISSN: 1040-4651.

[57] Nihal Dharmasiri, Sunethra Dharmasiri, and Mark Estelle. "The F-box protein TIR1 is an auxin receptor." In: *Nature* 435.7041 (May 2005), pp. 441–5. ISSN: 1476-4687.

[58] Stefan Kepinski and Ottoline Leyser. "The Arabidopsis F-box protein TIR1 is an auxin receptor." In: *Nature* 435.7041 (May 2005), pp. 446–51. ISSN: 1476-4687.

[59] Luz Irina A Calderón Villalobos et al. "A combinatorial TIR1/AFB-Aux/IAA co-receptor system for differential sensing of auxin." In: *Nature chemical biology* 8.5 (May 2012), pp. 477–85. ISSN: 1552-4469.

[60] W M Gray et al. "Auxin regulates SCF(TIR1)-dependent degradation of AUX/IAA proteins." In: *Nature* 414.6861 (Nov. 2001), pp. 271–6. ISSN: 0028-0836.

[61] Teva Vernoux et al. “The auxin signalling network translates dynamic input into robust patterning at the shoot apex.” In: *Molecular Systems Biology* 7 (Jan. 2011), p. 508. ISSN: 1744-4292.

[62] Géraldine Brunoud et al. “A novel sensor to map auxin response and distribution at high spatio-temporal resolution.” In: *Nature* 482.7383 (Feb. 2012), pp. 103–6. ISSN: 1476-4687.

[63] R Hertel, K S Thomson, and V E Russo. “In vitro auxin binding toparticulate cell fractions from corn coleoptiles.” In: *Planta* 107.4 (Dec. 1972), pp. 325–40. ISSN: 0032-0935.

[64] A M Jones. “Auxin-Dependent Cell Expansion Mediated by Overexpressed Auxin-Binding Protein 1”. In: *Science* 282.5391 (Nov. 1998), pp. 1114–1117.

[65] J G Chen et al. “ABP1 is required for organized cell elongation and division in Arabidopsis embryogenesis.” In: *Genes & Development* 15.7 (Apr. 2001), pp. 902–11. ISSN: 0890-9369.

[66] Nils Braun et al. “Conditional repression of AUXIN BINDING PROTEIN1 reveals that it coordinates cell division and cell expansion during postembryonic shoot development in Arabidopsis and tobacco.” In: *The Plant cell* 20.10 (2008), pp. 2746–62. ISSN: 1040-4651.

[67] Karine M David et al. “The auxin-binding protein 1 is essential for the control of cell cycle.” In: *The Plant Journal* 50.2 (Apr. 2007), pp. 197–206. ISSN: 0960-7412.

[68] Alexandre Tromas et al. “The AUXIN BINDING PROTEIN 1 is required for differential auxin responses mediating root growth.” In: *PloS ONE* 4.9 (Jan. 2009). Ed. by Edward Newbigin, e6648. ISSN: 1932-6203.

[69] Tongda Xu et al. “Cell surface- and rho GTPase-based auxin signaling controls cellular interdigitation in Arabidopsis.” In: *Cell* 143.1 (Oct. 2010), pp. 99–110. ISSN: 1097-4172.

[70] Yunus Effendi et al. “The heterozygous abp1/ABP1 insertional mutant has defects in functions requiring polar auxin transport and in regulation of early auxin-regulated genes.” In: *The Plant Journal* 65.2 (Jan. 2011), pp. 282–94. ISSN: 1365-313X.

[71] Melanie Monroe-Augustus, Bethany K Zolman, and Bonnie Bartel. “IBR5, a dual-specificity phosphatase-like protein modulating auxin and abscisic acid responsiveness in Arabidopsis.” In: *The Plant Cell* 15.12 (Dec. 2003), pp. 2979–91. ISSN: 1040-4651.

[72] D Reinhardt, T Mandel, and C Kuhlemeier. “Auxin regulates the initiation and radial position of plant lateral organs.” In: *The Plant cell* 12.4 (Apr. 2000), pp. 507–18. ISSN: 1040-4651.

[73] K. Okada et al. “Requirement of the Auxin Polar Transport System in Early Stages of Arabidopsis Floral Bud Formation.” In: *The Plant Cell* 3.7 (July 1991), pp. 677–684. ISSN: 1040-4651.

[74] Eva Benková et al. “Local, efflux-dependent auxin gradients as a common module for plant organ formation.” In: *Cell* 115.5 (Nov. 2003), pp. 591–602. ISSN: 0092-8674.

[75] Didier Reinhardt et al. “Regulation of phyllotaxis by polar auxin transport.” In: *Nature* 426.6964 (Nov. 2003), pp. 255–60. ISSN: 1476-4687.

[76] Pierre Barbier de Reuille et al. “Computer simulations reveal properties of the cell-cell signaling network at the shoot apex in Arabidopsis.” In: *Proceedings of the National Academy of Science of the United States of America* 103.5 (Jan. 2006), pp. 1627–32. ISSN: 0027-8424.

[77] Wim Grunewald and Jirí Friml. “The march of the PINs: developmental plasticity by dynamic polar targeting in plant cells.” In: *The EMBO Journal* 29.16 (Aug. 2010), pp. 2700–14. ISSN: 1460-2075.

[78] Marcus G Heisler et al. “Patterns of auxin transport and gene expression during primordium development revealed by live imaging of the Arabidopsis inflorescence meristem.” In: *Current biology* 15.21 (Nov. 2005), pp. 1899–911. ISSN: 0960-9822.

[79] Jennifer C Fletcher. “Shoot and floral meristem maintenance in arabidopsis.” In: *Annual review of plant biology* 53 (Jan. 2002), pp. 45–66. ISSN: 1543-5008.

[80] L Dolan et al. “Cellular organisation of the Arabidopsis thaliana root.” In: *Development* 119.1 (Sept. 1993), pp. 71–84. ISSN: 0950-1991.

[81] W. Boerjan. “superroot, a Recessive Mutation in Arabidopsis, Confers Auxin Overproduction”. In: *The Plant Cell* 7.9 (Sept. 1995), pp. 1405–1419. ISSN: 10404651.

[82] J E Malamy and P N Benfey. “Organization and cell differentiation in lateral roots of Arabidopsis thaliana.” In: *Development* 124.1 (Jan. 1997), pp. 33–44. ISSN: 0950-1991.

[83] J L Celenza, P L Grisafi, and G R Fink. “A pathway for lateral root formation in Arabidopsis thaliana.” In: *Genes & Development* 9.17 (Sept. 1995), pp. 2131–42. ISSN: 0890-9369.

[84] Franck Anicet Ditengou et al. “Mechanical induction of lateral root initiation in Arabidopsis thaliana.” In: *Proceedings of the National Academy of Sciences of the United States of America* 105.48 (Dec. 2008), pp. 18818–23. ISSN: 1091-6490.

[85] M Lucas et al. “Auxin fluxes in the root apex co-regulate gravitropism and lateral root initiation.” In: *Journal of Experimental Botany* 59.1 (Jan. 2008), pp. 55–66. ISSN: 1460-2431.

[86] Ive De Smet et al. "Auxin-dependent regulation of lateral root positioning in the basal meristem of Arabidopsis." In: *Development* 134.4 (Feb. 2007), pp. 681–90. ISSN: 0950-1991.

[87] Bernadette Guenot et al. "Pin1-independent leaf initiation in Arabidopsis." In: *Plant Physiology* 159.4 (Aug. 2012), pp. 1501–10. ISSN: 1532-2548.

[88] Taylor A. Steeves and Ian M. Sussex. *Patterns in Plant Development.* 2nd Editio. Cambridge, England, 1989, p. 408. ISBN: 9780521288958.

[89] Marta Ibañes et al. "Brassinosteroid signaling and auxin transport are required to establish the periodic pattern of Arabidopsis shoot vascular bundles." In: *Proceedings of the National Academy of Sciences of the United States of America* 106.32 (Aug. 2009), pp. 13630–5. ISSN: 1091-6490.

[90] Idan Efroni et al. "A protracted and dynamic maturation schedule underlies Arabidopsis leaf development." In: *The Plant cell* 20.9 (Sept. 2008), pp. 2293–306. ISSN: 1040-4651.

[91] Nancy G Dengler and Hirokazu Tsukaya. *Leaf Morphogenesis in Dicotyledons: Current Issues.* 2001.

[92] P M Donnelly et al. "Cell cycling and cell enlargement in developing leaves of Arabidopsis." In: *Developmental biology* 215.2 (Nov. 1999), pp. 407–19. ISSN: 0012-1606.

[93] Kiu Hyung Cho et al. "Developmental processes of leaf morphogenesis inarabidopsis". In: *Journal of Plant Biology* 50.3 (June 2007), pp. 282–290. ISSN: 1226-9239.

[94] Eiko Kawamura, Gorou Horiguchi, and Hirokazu Tsukaya. "Mechanisms of leaf tooth formation in Arabidopsis." In: *The Plant journal* 1 (Mar. 2010), pp. 429–441. ISSN: 1365-313X.

[95] Gemma D Bilsborough et al. "Model for the regulation of Arabidopsis thaliana leaf margin development." In: *Proceedings of the National Academy of Sciences of the United States of America* 108.8 (Feb. 2011), pp. 3424–9. ISSN: 1091-6490.

[96] Carol L Wenzel et al. "Dynamics of MONOPTEROS and PIN-FORMED1 expression during leaf vein pattern formation in Arabidopsis thaliana." In: *The Plant journal : for cell and molecular biology* 49.3 (Mar. 2007), pp. 387–98. ISSN: 0960-7412.

[97] T. Sachs. "Polarity and the Induction of Organized Vascular Tissues". In: *Annals of Botany* 33.2 (Mar. 1969), pp. 263–275.

[98] G. J. Mitchison. "A Model for Vein Formation in Higher Plants". In: *Proceedings of the Royal Society B: Biological Sciences* 207.1166 (Feb. 1980), pp. 79–109. ISSN: 0962-8452.

[99] G. J. Mitchison, D. E. Hanke, and A. R. Sheldrake. “The Polar Transport of Auxin and Vein Patterns in Plants [and Discussion]”. In: *Philosophical Transactions of the Royal Society B: Biological Sciences* 295.1078 (Oct. 1981), pp. 461–471. ISSN: 0962-8436.

[100] Hironori Fujita and Atsushi Mochizuki. “Pattern formation of leaf veins by the positive feedback regulation between auxin flow and auxin efflux carrier.” In: *Journal of Theoretical Biology* 241.3 (Aug. 2006), pp. 541–51. ISSN: 0022-5193.

[101] François G Feugier and Yoh Iwasa. “How canalization can make loops: a new model of reticulated leaf vascular pattern formation.” In: *Journal of Theoretical Biology* 243.2 (Nov. 2006), pp. 235–44. ISSN: 0022-5193.

[102] K Alim and E Frey. “Quantitative predictions on auxin-induced polar distribution of PIN proteins during vein formation in leaves.” In: *The European Physical Journal. E, Soft Matter* 33.2 (Oct. 2010), pp. 165–73. ISSN: 1292-895X.

[103] Francois G Feugier, A Mochizuki, and Y Iwasa. “Self-organization of the vascular system in plant leaves: inter-dependent dynamics of auxin flux and carrier proteins.” In: *Journal of Theoretical Biology* 236.4 (Oct. 2005), pp. 366–75. ISSN: 0022-5193.

[104] Szymon Stoma et al. “Flux-based transport enhancement as a plausible unifying mechanism for auxin transport in meristem development.” In: *PLoS Computational Biology* 4.10 (Oct. 2008), e1000207. ISSN: 1553-7358.

[105] Richard S Smith et al. “A plausible model of phyllotaxis.” In: *Proceedings of the National Academy of Sciences* 103.5 (Jan. 2006), pp. 1301–6. ISSN: 0027-8424.

[106] Alan C Newell, Patrick D Shipman, and Zhiying Sun. “Phyllotaxis: cooperation and competition between mechanical and biochemical processes.” In: *Journal of Theoretical Biology* 251.3 (2008), pp. 421–39. ISSN: 1095-8541.

[107] Henrik Jönsson et al. “An auxin-driven polarized transport model for phyllotaxis.” In: *Proceedings of the National Academy of Sciences* 103.5 (Jan. 2006), pp. 1633–8. ISSN: 0027-8424.

[108] Roeland M H Merks et al. “Canalization without flux sensors: a traveling-wave hypothesis.” In: *Trends in Plant Science* 12.9 (Sept. 2007), pp. 384–90. ISSN: 1360-1385.

[109] Emmanuelle M Bayer et al. “Integration of transport-based models for phyllotaxis and midvein formation.” In: *Genes & Development* 23.3 (Feb. 2009), pp. 373–84. ISSN: 1549-5477.

[110] Marcus G. Heisler et al. "Alignment between PIN1 Polarity and Microtubule Orientation in the Shoot Apical Meristem Reveals a Tight Coupling between Morphogenesis and Auxin Transport". In: *PLoS Biology* 8.10 (Oct. 2010). Ed. by Ottoline Leyser, e1000516. ISSN: 1545-7885.

[111] Gerardo Tauriello and Petros Koumoutsakos. "Coupling Remeshed Particle and Phase Field Methods for the Simulation of Reaction-Diffusion on the Surface and the Interior of Deforming Geometries". en. In: *SIAM Journal on Scientific Computing* 35.6 (Jan. 2013), B1285–B1303. ISSN: 1064-8275.

[112] Johannes Schindelin et al. "Fiji: an open-source platform for biological-image analysis." In: *Nature Methods* 9.7 (July 2012), pp. 676–82. ISSN: 1548-7105.

[113] Daniel Kierzkowski et al. "Elastic domains regulate growth and organogenesis in the plant shoot apical meristem." In: *Science* 335.6072 (Mar. 2012), pp. 1096–9. ISSN: 1095-9203.

[114] Romain Fernandez et al. "Imaging plant growth in 4D: robust tissue reconstruction and lineaging at cell resolution." In: *Nature Methods* May (June 2010). ISSN: 1548-7105.

[115] Tony J Collins. "ImageJ for microscopy". In: *BioTechniques* 43.S1 (2007), S25–S30.

[116] Bruce E Shapiro, Elliot M Meyerowitz, and Eric Mjolsness. "Using cellzilla for plant growth simulations at the cellular level." In: *Frontiers in plant science* 4 (Jan. 2013), pp. 1–9. ISSN: 1664-462X.

[117] Bruce E Shapiro et al. "Cellerator: extending a computer algebra system to include biochemical arrows for signal transduction simulations." In: *Bioinformatics (Oxford, England)* 19.5 (Mar. 2003), pp. 677–8. ISSN: 1367-4803.

[118] Maruthachalam Ravi and Simon W L Chan. "Haploid plants produced by centromere-mediated genome elimination." In: *Nature* 464.7288 (Mar. 2010), pp. 615–8. ISSN: 1476-4687.

[119] Hirokazu Tsukaya. "Mechanism of leaf-shape determination." In: *Annual review of plant biology* 57 (Jan. 2006), pp. 477–96. ISSN: 1543-5008.